

Supporting Information
for

A fluorinated zirconium-based metal-organic framework as a platform for the capture and removal of perfluorinated pollutants from air and water

Daniel Hedbom, Philipp Gaiser, Tyran Günther, Michelle Åhlén, Ocean Cheung, Maria Strømme, Michelle Åhlén* and Martin Sjödin*

Division of Nanotechnology and Functional Materials, Department of Materials Science and Engineering, Uppsala University, Ångström Laboratory, Uppsala SE-751 03, BOX 35, Sweden.

E-mail : Martin.Sjodin@angstrom.uu.se

Michelle.Ahlen@angstrom.uu.se

Table of contents

S 1. Materials	S-3
S 2. Synthesis details	S-3
S 2.1. Synthesis of UiO-67	S-3
S 2.2. Synthesis of UiO-67-F2 ($[Zr_6O_4(OH)_4(bpdc-F_2)_6]$)	S-3
S 2.3. Synthesis of UiO-67-NH ₂ ($[Zr_6O_4(OH)_4(bpdc-NH_2)_6]$)	S-3
S 2.4. Synthesis of UiO-68-(CF ₃) ₂ ($[Zr_6O_4(OH)_4(tpdc-(CF_3)_2)_6]$)	S-3
S 3. Powder X-ray Diffraction	S-4
S 3.1. Pawley and Rietveld refinement.....	S-4
S 4. X-Ray photoelectron spectroscopy (XPS)	S-8
S 5. Fourier transform infrared spectroscopy.....	S-9
S 6. Thermogravimetric analysis	S-10
S 7. Stability study.....	S-12
S 8. Scanning Electron Microscopy images.....	S-12
S 9. Energy-dispersive X-Ray spectroscopy.....	S-13
S 9.1. EDX maps of UiO-67	S-14
S 9.2. EDX maps of UiO-67-NH ₂	S-15
S 9.3. EDX maps of UiO-67-2F	S-16
S 9.4. EDX maps of UiO-68-(CF ₃) ₂	S-17
S 10. Scanning Transmission electron microscopy (STEM).....	S-18
S 10.1 Energy dispersive X-Ray spectroscopy (STEM-EDX).....	S-19
S 11. Transmission electron microscopy (TEM).....	S-20
S 12. Gas sorption.....	S-20
S 13. Isosteric enthalpy of adsorption.....	S-28
S 13.1. Isosteric enthalpy of CO ₂ adsorption.....	S-30
S 13.2. Isosteric enthalpy of CH ₄ adsorption	S-34
S 13.3. Isosteric enthalpy of SF ₆ adsorption	S-37
S 14. Ideal Adsorbed Solution Theory	S-40
S 15. Ideal selectivity.....	S-41
S 16. Summary of sorption properties	S-43
S 17. PFOA adsorption.....	S-45
References.....	S-52

S 1. Materials

N, N-Dimethylformamide (DMF) ≥99.5%, GPR RECTAPUR and **Ethanol Absolute Ph. Eur** (99.7%) (Solveco) were purchased from VWR international and **Zirconium (IV) chloride** (ZrCl_4), (99.5%+) (metals basis) Reactor grade was purchased from Thermo Scientific. **Benzoic acid** Reagent plus® (99%), **Deuterium oxide** (D_2O) 99.9%, **Perfluorooctanoic acid** (PFOA) 95%, and **2,2,2-Trifluoroethanol** >99% were purchased from Sigma-Aldrich. **[1,1'-Biphenyl]-4,4'-dicarboxylic acid** (H_2bpdc) (97%), **3,3'-difluoro-[1,1'-biphenyl]-4,4'-dicarboxylic acid** ($\text{H}_2\text{bpdc-F}_2$) (97%), and **2',5'-Bis(trifluoromethyl)-[1,1':4',1"-terphenyl]-4,4"-dicarboxylic acid** (95%) ($\text{H}_2\text{tpdc-(CF}_3)_2$) was purchased from BLD Pharma. **2-Amino-4,4'-biphenyl dicarboxylic acid** ($\text{H}_2\text{bpdc-NH}_2$) (>97%) was purchased from Shanghai Tensus Biotech Co., Ltd. and.

All chemicals were used as delivered, without further purification aside from which DMF was dried and stored with 4A activated zeolite molecular sieves.

S 2. Synthesis details

All metal-organic framework materials were synthesized with DMF dried and stored over activated 3 Å molecular sieves.

S 2.1. Synthesis of UiO-67

The synthesis of UiO-67 was performed according to a previously published route by Stanley et.al.¹. In a flame dried round flask, 126 mg (0.54 mmol) ZrCl_4 was dissolved in 5 mL DMF and 1 mL HCl (fuming) after which 10 mL DMF was added followed by 150 mg (0.62 mmol) H_2bpdc . The suspension was sonicated for 20 min and thereafter heated at 80 °C for 24 h. The resulting white powder was washed three times with 35 mL DMF, 35 mL ethanol, and finally dried at 70 °C in a ventilated oven overnight.

S 2.2. Synthesis of UiO-67-F2 ($[\text{Zr}_6\text{O}_4(\text{OH})_4(\text{bpdc-F}_2)_6]$)

37.3 mg (0.16 mmol) ZrCl_4 was combined with 393 mg (3.22 mmol) of benzoic acid and 6.25 mL dried DMF in a glass vial. This mixture was sonicated for 15 min after which 8.75 µL distilled H_2O was added and vial vortexed. 72.7 mg (0.16 mmol) $\text{H}_2\text{bpdc-F}_2$ was added and the mixture was sonicated for 15 min. The solution was transferred to a PTFE insert in a stainless-steel autoclave and placed in a 120 °C preheated oven for 72 h. The resulting suspension was separated using a centrifuge and the product was washed three times with 35 mL DMF, 35 mL ethanol, and subsequently dried overnight in a ventilated oven at 70 °C.

S 2.3. Synthesis of UiO-67-NH2 ($[\text{Zr}_6\text{O}_4(\text{OH})_4(\text{bpdc-NH}_2)_6]$)

The synthesis of UiO-67-NH2 was performed in a slightly modified way to previously published procedures by Kaur et al.². Briefly, 901.86 mg (3.87 mmol) ZrCl_4 and 1 417 mg (11.6 mmol) benzoic acid were combined in 15 mL DMF and dissolved by sonication. 995.52 mg (3.87 mmol) (3.87 mmol) $\text{H}_2\text{bpdc-NH}_2$ was thereafter added together with 8.5 µL distilled H_2O and further sonicated for 15 min, after which the opaque mixture was refluxed at 130 °C for 24 h. The obtained product was washed three times in 35 mL DMF and 35 mL ethanol and dried overnight in ventilated oven at 70 °C.

S 2.4. Synthesis of UiO-68-(CF₃)₂ ($[\text{Zr}_6\text{O}_4(\text{OH})_4(\text{tpdc-(CF}_3)_2)_6]$)

The synthesis of UiO-68-(CF₃)₂ was performed according to a previously published procedure by Wang et al.³. Briefly, 12.5 mL DMF, 36.4 mg (0.16 mmol) ZrCl_4 , and 781 mg (6.40 mmol) benzoic acid were combined under sonication for 20 min. 70.99 mg (0.16 mmol) $\text{H}_2\text{tpdc-(CF}_3)_2$

was added and the mixture was further sonicated for 15 min. This solution was placed into a PTFE insert in a stainless-steel autoclave and left at 130 °C in a preheated oven for 74 h. The resulting white powder was washed three times with 35 mL DMF, 35 mL ethanol, and finally dried at 70 °C in a ventilated oven overnight.

S 3. Powder X-ray Diffraction

Powder X-ray diffractograms were recorded on a Bruker D8 Advance with Twin/Twin optics (Bremen, Germany) using Cu K_α ($\lambda = 1.5406 \text{ \AA}$) radiation on a rotating zero-background plate sample holder on a modified Bruker D8 equipped with a Lynxeye-XE-T detector (Bremen, Germany), using a variable detector window, a beam knife, and a zero-background plate. The voltage used was 40 kV, the current 40 mA with a 0.0205° step size, under ambient conditions. The Pawley fit of UiO-67-NH₂ and UiO-68-(CF₃)₂ was performed using jEdit (General Public License) and TOPAS 6 (Bruker AXS). Capillary PXRD-data of UiO-67-F2 was gathered, the configuration was a Debye-Scherer 1 mm diameter, glass capillary. A fully degassed sample were packed into a capillary tube, which was glued-shut using epoxy resin. The sample was analysed on a Bruker D8 advance (Bremen, Germany) with a 40 kV, 40 mA Cu K_α ($\lambda = 1.5406 \text{ \AA}$) radiation source, and a Lynxeye XE-T detector between 3 – 90 2θ (°). The step size was 0.0202° (4 308 steps) with 3 072 s/step (for a total of 20.04 h). All PXRD were gathered under ambient atmosphere and temperature.

S 3.1. Pawley and Rietveld refinement

Pawley fittings and Rietveld refinement (Figs S1 – S3 and Table S1). were performed in jEdit (General Public License) and TOPAS 6 (Bruker AXS). The fits were improved upon until a R_{wp} of 7.99 % (R_{exp}/R_1 of 4.29%) was reached. As can be seen in Figs S1 – S3, most of the error was derived from the peak shape/ axial divergence which were located at low 2θ (°). Rietveld refinement of UiO-67-F2 ⁴ (Table S1) was carried out suing a Thompson-Cox-Hastings pseudo-Voigt peak shape (TCHZ). Grain size parameters were left open to refine as the samples were nanoparticulate and the crystal size greatly contributed to broadening. Cylindrical sample correction was used (which accounted for errors in capillary mounting). Atomic displacement parameters were confined to below 5 and occupancy below or equal to one. Fluorine occupancy was confined to below or equal to 0.250 due to symmetry equivalents. The refinement was limited to a 2θ range of 4 – 46 °, this limit was set due to low peak-to-noise ratio at higher angles. As the included range was limited, thermal displacement parameters did not converge. Furthermore, Zr and O1 positions were allowed fitting.

Pawley refinements were improved upon only to the point of confirming no missing intensities and improved unit cell parameters. Thompson-Cox-Hastings pseudo-Voigt peak shapes were selected.

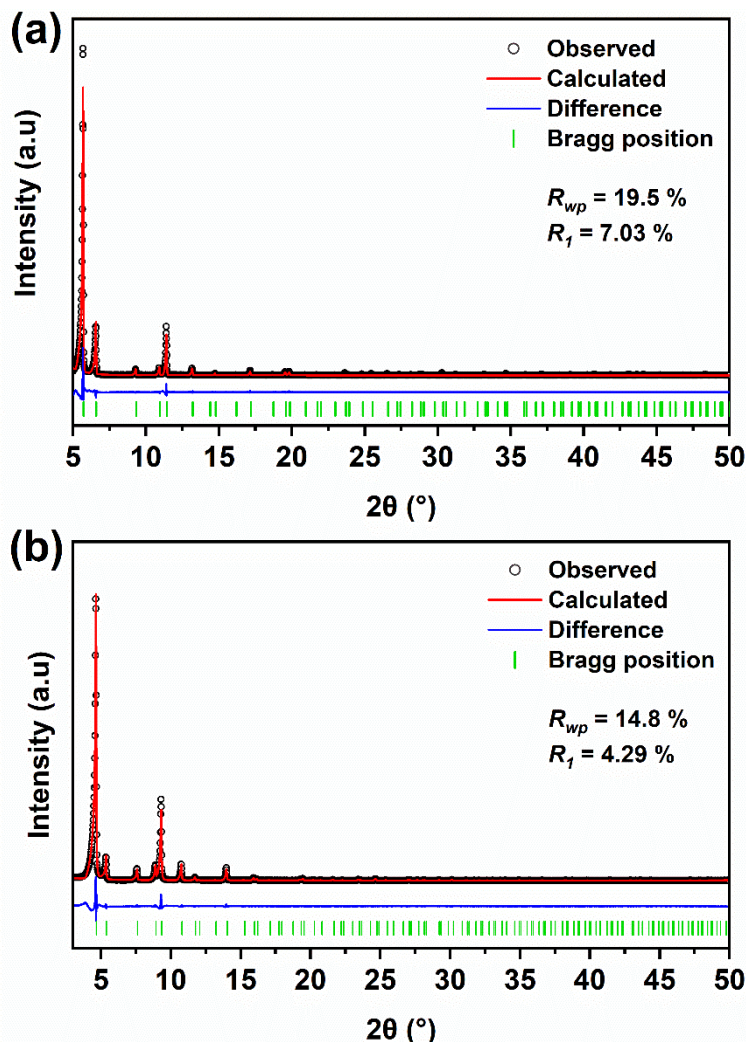


Fig S1. Pawley fits of (a) UiO-67-NH_2 , and (b) $\text{UiO-68-(CF}_3)_2$.

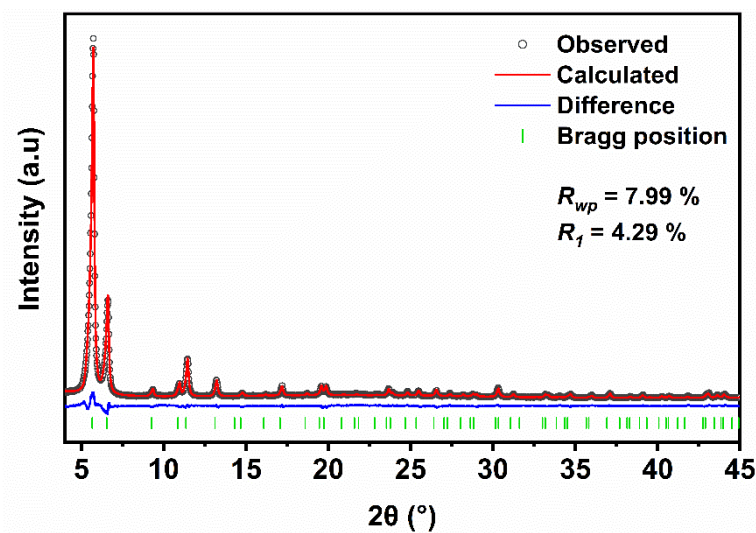


Fig S2. Rietveld fit of UiO-67-F_2 .

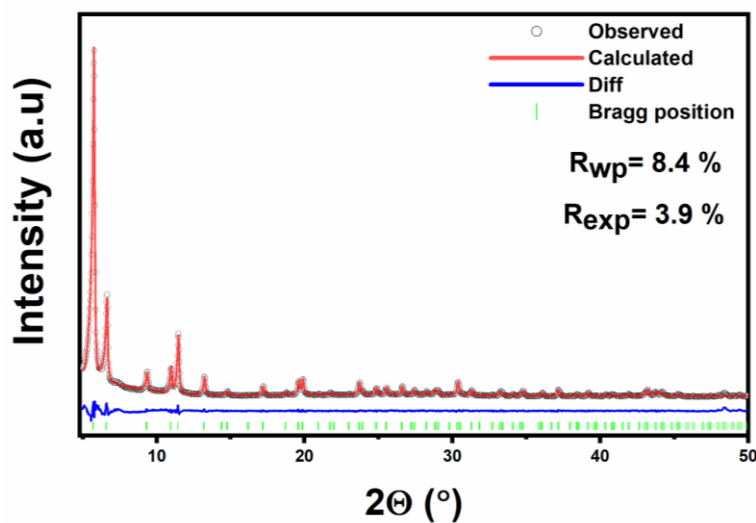


Fig S3. Pawley fit of UiO-67.

Table S1. Refinement parameters and details for UiO-67-F2, UiO-67-NH₂, UiO-68-(CF₃)₂, and UiO-67.

	UiO-67-F2	UiO-67-NH ₂	UiO-68-(CF ₃) ₂	UiO-67
Crystal system	Cubic	Cubic	Cubic	Cubic
Space group	<i>Fm-3m</i> (No. 225)	<i>Fm-3m</i> (No. 225)	<i>Fm-3m</i> (No. 225)	<i>Fm-3m</i> (No. 225)
a = b = c (Å)	26.981	26.842	32.849	26.832
Z	4	4	4	4
Volume (Å³)	19 642	18 961	35 445	19 318
Calc. density (cm³ g⁻¹)	0.790	0.764	0.649	0.741
Temperature (K)	298 K	298 K	298 K	298 K
R_{wp} (%)	7.99	19.50	14.8	8.4
R₁ (%)	4.29	7.03	3.78	3.9
GoF	1.86	3.13	3.91	2.1
Source	Cu K _α (λ = 1.5406 Å)	Cu K _α (λ = 1.5406 Å)	Cu K _α (λ = 1.5406 Å)	Cu K _α (λ = 1.5406 Å)
Refinement	Rietveld	Pawley	Pawley	Pawley

Table S2 Atomic parameters of UIO-67-F2-obtained from Rietveld refinement.

Atom	Site	x	y	z	Occupancy	U_{eq}
Zr	Zr	0.0917	0.00000	0.0000	0.9999	1.1439
O	O1	0.0464	0.04639	0.0464	0.9994	0.1226
O	O2	0.1326	0.00000	0.0719	0.9999	0.7526
C	C1	0.1172	0.00000	0.1172	1	4.9945
C	C2	0.1565	0.00000	0.1565	1	4.9994
C	C3	0.2058	0.00000	0.1447	0.9864	4.9987
F	F1	0.2149	0.00000	0.1114	0.25	5
C	C4	0.2420	0.00000	0.1795	0.8967	4.9987
C	C5	0.2307	0.00000	0.2307	0.9998	4.9987

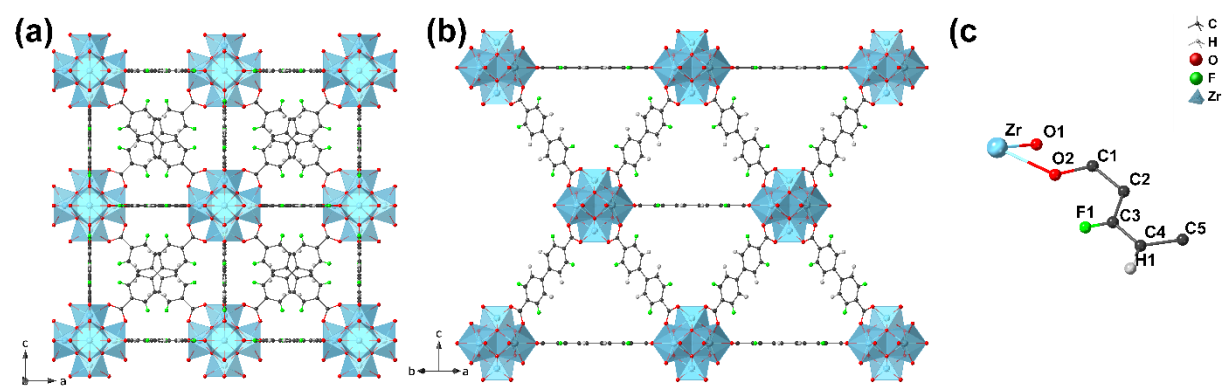


Fig. S4 Crystal structure of UIO-67-F2 as viewed along (a) [100], (b) [111], and (c) the asymmetric unit. No solvent molecules were located during refinement (no SQUEEZE was used).

S 4. X-Ray photoelectron spectroscopy (XPS)

X-ray photoelectron spectroscopy was captured using a Physical Electronics (PHI) Quantera II XPS using a scanning XPS Microprobe.

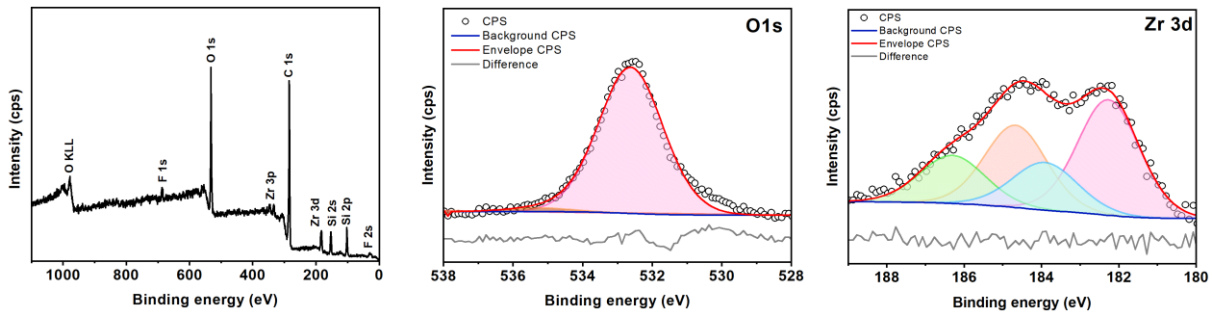


Fig S5. XPS (left) survey spectrum and high-resolution spectra for (middle) O 1s and (right) Zr 3d of UiO-67-2F.

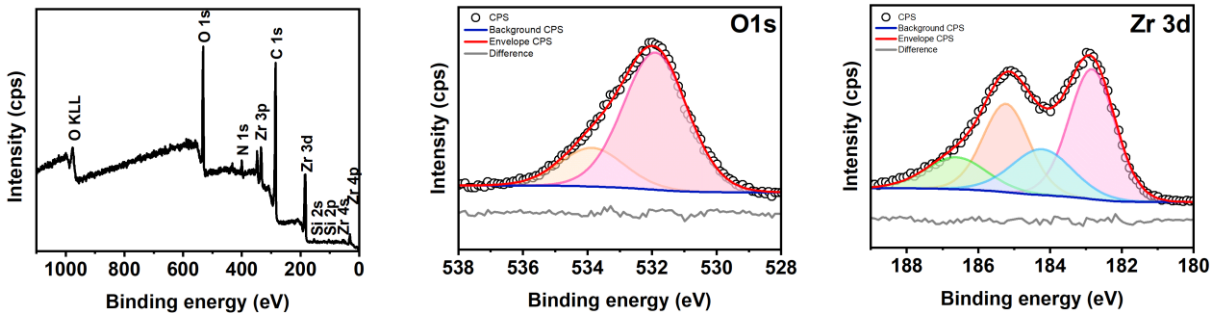


Fig S6. XPS (left) survey spectrum and high-resolution spectra for (middle) O 1s and (right) Zr 3d of UiO-67-NH₂.

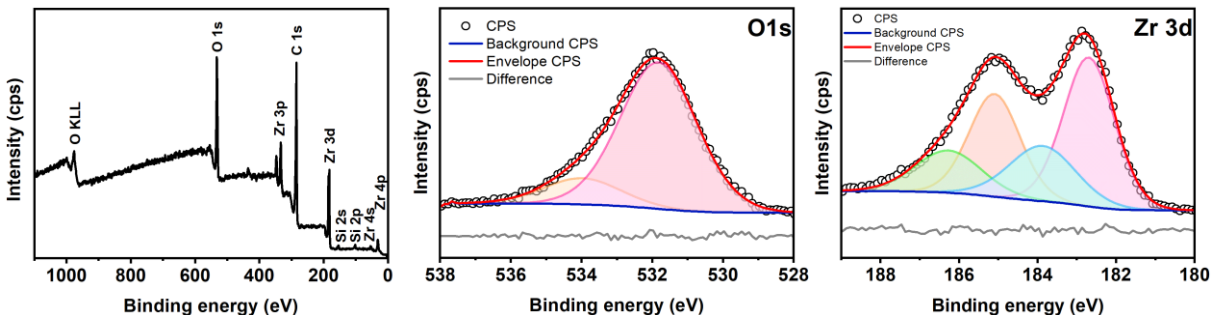


Fig S7. XPS (left) survey spectrum and high-resolution spectra for (middle) O 1s and (right) Zr 3d of UiO-67.

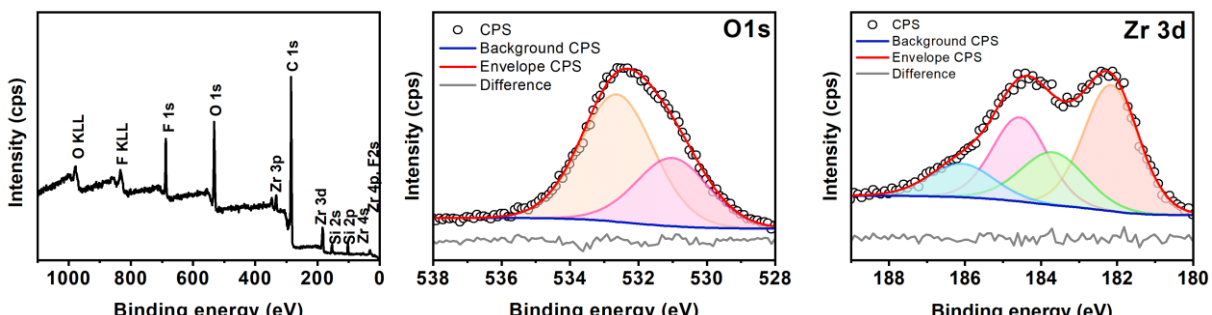


Fig S8. XPS (left) survey spectrum and high-resolution spectra for (middle) O 1s and (right) Zr 3d of UiO-68-(CF₃)₂.

S 5. Fourier transform infrared spectroscopy

Fourier transform infrared spectroscopy (FT-IR) spectra of the UiO-MOFs were collected on a Bruker Tensor 27 FT-IR spectrometer (Bremen, Germany) with an ATR unit.

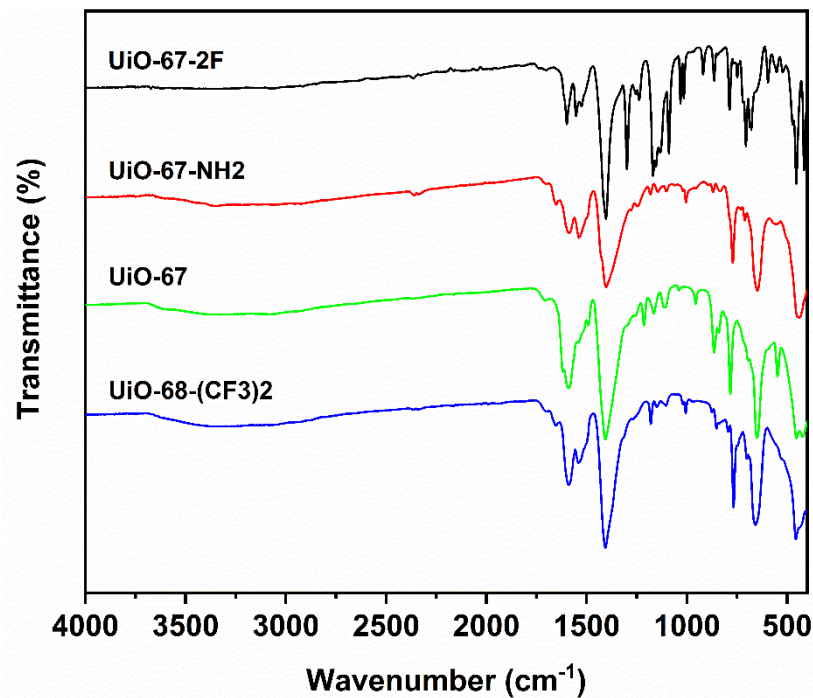


Fig S9. FTIR spectra of as-synthesized UiO-MOFs.

S 6. Thermogravimetric analysis

Thermogravimetric decomposition profile was recorded using a Mettler Toledo Thermal Analysis System TGA/DSC 3+ (Columbus, OH, USA) at a heating rate of 10 °C/min in air (60 ml/min). Samples from UiO-67, UiO-67-F2, and UiO-67-NH₂ were fully decomposed by heating the samples from 25 – 200 °C and 200 – 800 °C. All samples were shifted so as to show the final plateau corresponding to pure ZrO₂ as “100%”.

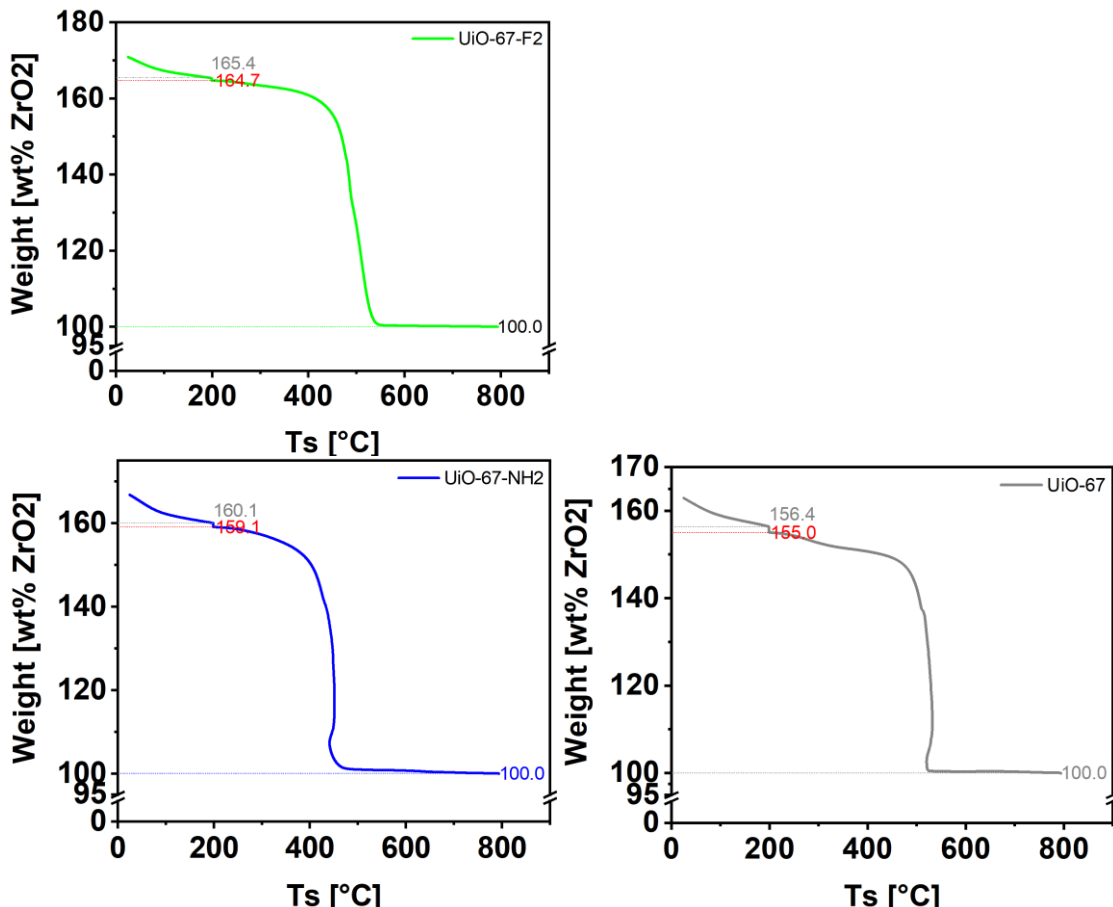


Fig S10. Decomposition profiles of UiO-67-F2, UiO-67-NH₂, and UiO-67. Red index is the plateau corresponding to a fully dehydroxylated MOF and the grey index corresponds to the mass before the 2h hold at 200 °C.

Using a method published by Lillerud et.al.⁵

The theoretical mass-platforms where the hypothetical, defect free MOF should be, should be at,

$$\text{Zr}_6\text{O}_4 \text{ (Linker)}_6 [\text{ZrO}_2 \text{ wt\%}] = \frac{M_{\text{dehydroxylatedMOF}}}{6 * M_{\text{ZrO}_2}}$$

$$\text{Experimental } \text{Zr}_6\text{O}_4 \text{ (Linker)}_6 [\text{ZrO}_2 \text{ wt\%}] = \frac{w\text{t}_{200} - w\text{t}_{800}}{6}$$

The number of defects (indistinguishable from organic counter ions within UiO-67-F2), is therefore observed to be

$$x_{\text{UiO-67-F2}} = 6 - n_{\text{expected}}[\#] = \frac{wt_{200} - wt_{800}[\text{ZrO}_2 \text{ wt\%}]}{\text{Zr}_6\text{O}_4 \text{ (Linker)}_6 [\text{ZrO}_2 \text{ wt\%}]} = 6 - \left(\frac{164.7 - 100}{\frac{307\% - 100\%}{6}} \right) = \dots$$

Where wt_{200} is the experimental mass at 200 C wt_{800} is the experimental mass at 800 C. $\text{Zr}_6\text{O}_4(\text{Linker})_6$ is the difference between the theoretical defect free mass and the final mass at 800C divided by the formula unit number of Zr.

Similar calculations can be performed for UiO-67-NH₂ and UiO-67 (wt₂₀₀, wt₈₀₀ available below in Table S3), and the results of these calculations are available in Table S 16 2.

Table S3. Summary of results obtained from thermogravimetric analysis.

Sample	Experimental		Theoretical wt%, 200 °C (ZrO ₂ wt%)	Theoretical molar mass (g/mol)
	wt % 200 °C (ZrO ₂ wt%)	wt % 800 °C (ZrO ₂ wt%)		
UiO-67-F2	164.7	100	307	2268.49
UiO-67-NH ₂	159.1	100	290	2142.70
UiO-67	155.0	100	278	2052.61

Table S4. Comparative overview of the at% Zr ratios and Zr molar ratio from EDX and TGA, respectively.

Sample	EDX			TGA			
	Zr:F (at% Zr ratio)	Zr:N (at% Zr ratio)	Deficiency (at% ratio)	Zr:F (mol Zr ratio)	Zr:N (mol Zr ratio)	Zr:linker (mol ratio)	Deficiency (mol Zr ratio)
UiO-67- F2	1:1.4 (1:2)*	-	30 %	1:1.37 (1:2)*	-	6:4.12 (6:6)*	31 %
UiO-68- (CF ₃) ₂	1:4.9 (1:6)*	-	18 %	(1:6)*	-	-	-
UiO-67- NH ₂	-	1:0.8 (1:1)*	20 %	-	1:0.69 (1:1)*	6:4.13 (6:6)*	31 %
UiO-67	-	-	-	-	-	6:4.14 (6:6)*	31 %

* Ideal ratio.

Following are the same results presented in formula units,

- UiO-67-F2: $\text{Zr}_6\text{O}_{5.88} (\text{C}_{14}\text{H}_6\text{F}_2\text{O}_4)_{4.12}$
- UiO-67-NH₂: $\text{Zr}_6\text{O}_{5.87} (\text{C}_{14}\text{H}_9\text{N}_0\text{O}_4)_{4.13}$
- UiO-67: $\text{Zr}_6\text{O}_{5.86} (\text{C}_{14}\text{H}_8\text{O}_4)_{4.14}$

which in turn would mean dehydroxylated/hydrated molar masses of 1779.33, 1695.34, and 1635.57 g/mol for UiO-67-F2, UiO-67-NH₂, and UiO-67, respectively.

S 7. Stability study

The water stability of UiO-67-F2, UiO-67-NH₂, and UiO-67 were examined using TGA. The MOFs were placed in deionized water for 150 min, and dried overnight in a 70 °C ventilated oven. After this, the MOFs were degassed at 150 °C for 120 – 180 min (50 mL/min N₂ flow-rate) after which the samples were exposed to a CO₂ atmosphere (50 mL/min CO₂ flow-rate) at 30 °C (Fig S7).

As is visible in Fig S7 and Table S1, UiO-67-F2 shows no decrease in uptake capacity upon wetting. UiO-67 however, loses a great deal of its already low capacity upon wetting. As does UiO-68-(CF3)₂.

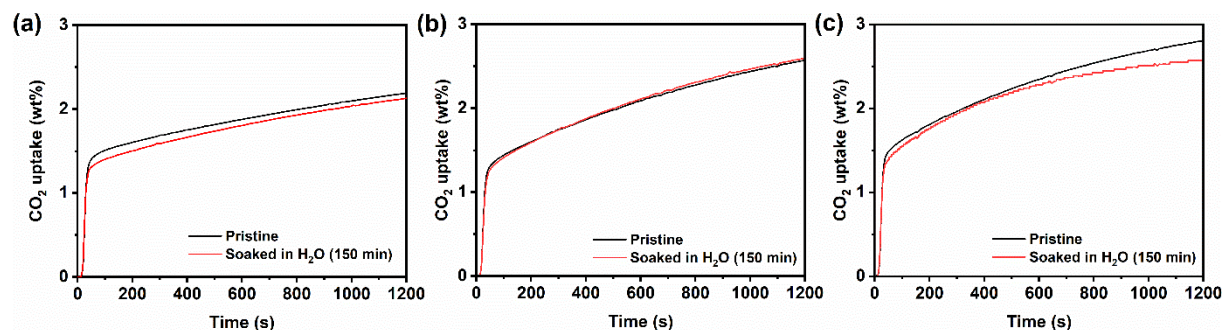


Fig S11. Gravimetric CO₂ adsorption profiles of pristine and H₂O-soaked samples of (a) UiO-67-F2, (b) UiO-67-NH₂, and (c) UiO-67.

Table S5. Summary of the gravimetric CO₂ uptake of UiO-MOFs.

Sample	Pristine		H ₂ O-soaked	
	CO ₂ uptake		CO ₂ uptake	
	(wt %)	(wt %)	(wt %)	(wt %)
UiO-67-F2	2.19		2.13	
UiO-67-NH ₂	2.61		2.59	
UiO-67	2.82		2.58	

S 8. Scanning Electron Microscopy images

Scanning electron microscopy (SEM) images were collected on a Zeiss Merlin High Resolution Scanning Electron Microscope (Oberkochen, Germany), at 1 kV and 25 pA. All samples were sputter coated with gold/palladium (~5 nm thick) using a polaron SC7640 (Quorum technologies, Kent, UK) at 2 kV and 20 mA for 40 s prior to imaging.

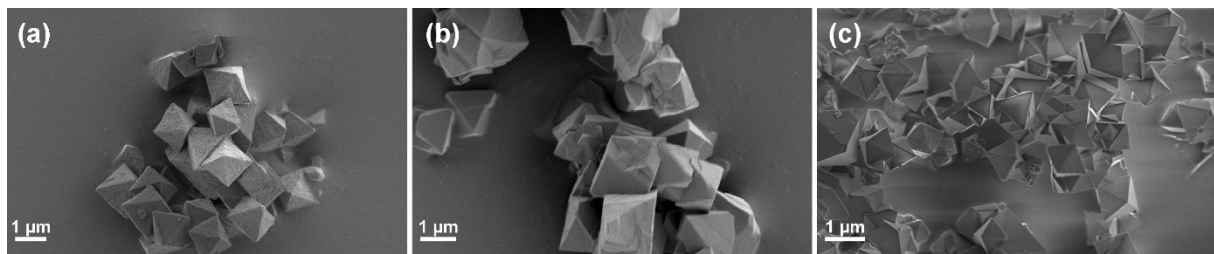


Fig S12. SEM images of (a) UiO-67-NH₂, (b) UiO-67-F2, and (c) UiO-68-(CF₃)₂. was performed on all samples at 1 kV and 25 pA with an in-lens detector. All samples were sputter coated with gold/palladium.

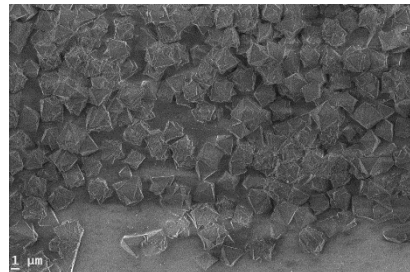
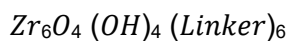


Fig S13. SEM image of UiO-67. Imaging was performed on all samples at 1 kV and 25 pA with an in-lens detector. The sample was sputter coated with gold/palladium.

S 9. Energy-dispersive X-Ray spectroscopy

SEM-energy-dispersive X-ray spectroscopy (EDX) was performed a Zeiss LEO 1330 Scanning Electron Microscope (Oberkochen, Germany) using an Oxford Instruments X-Max 80 mm² Silicon Drift Detector (Abingdon, UK) at 10 kV. The sampled area was approximately 50 000 μm². In a defect free structure, hydroxylated state, these materials should all have a formula unit similar to,



The quantities of O and C can unfortunately not be quantified with any certainty as the sample holders are composed of carbon, and any contaminants/adsorbed molecules are assumed to be unknowable amounts of hydrocarbons, water, or benzoic acid from the synthesis.

The functional groups in the cases of UiO-67-NH₂, UiO-67-F2, and UiO-68-(CF₃)₂ should represent some manner of defect as the hypothetical ratio between them is well defined. With the caution that they are heavy elements (Zr) in a matrix of light elements.

In the case of UiO-67-NH₂, the Zr:N should be 1:1 in atomic %, the explicit amounts are 4.98:4.10 (1:0.8), the defects present should be missing linkers as such. UiO-67-F2 should be Zr:F 1:2, experimentally it is 3.90:5.52 (1:1.4), the defects present should be missing linkers. In UiO-68-(CF₃)₂ the ideal ratio would be 1:6 (1:4.9). This of course, barring missing cluster-defects (where the hydroxylated zirconium SBU is missing with a number of linkers attached).

S 9.1. EDX maps of **UiO-67**

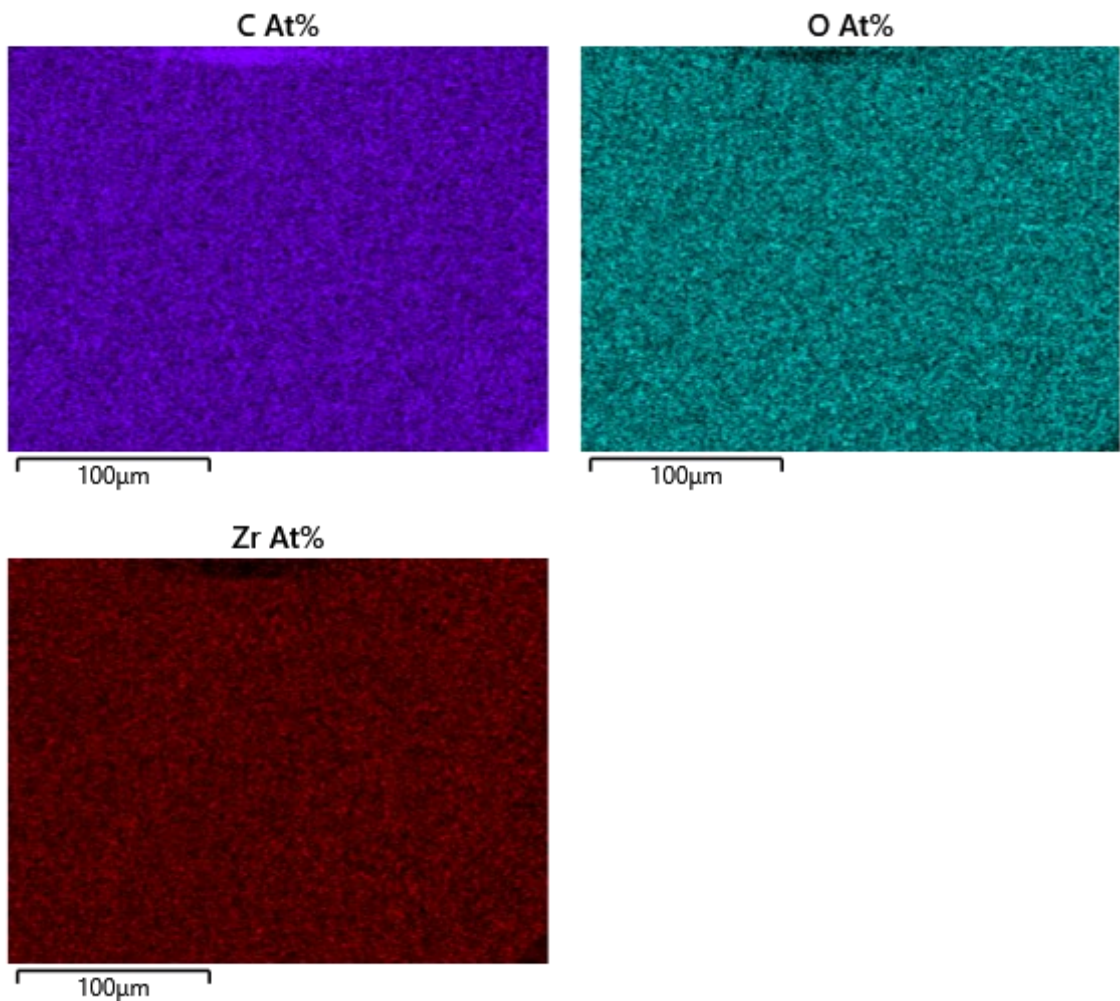


Fig S14. EDX maps of carbon (C), oxygen (O), and zirconium (Zr) from UiO-67.

Table S6. EDX map results in atomic %, of UiO-67.

Statistic	C (at %)	O (at %)	Zr (at %)
Max	76.95	29.83	2.54
Min	67.63	20.82	2.23
Average	72.29	25.33	2.38
Standard Deviation	6.59	6.37	0.22

S 9.2. EDX maps of UiO-67-NH₂

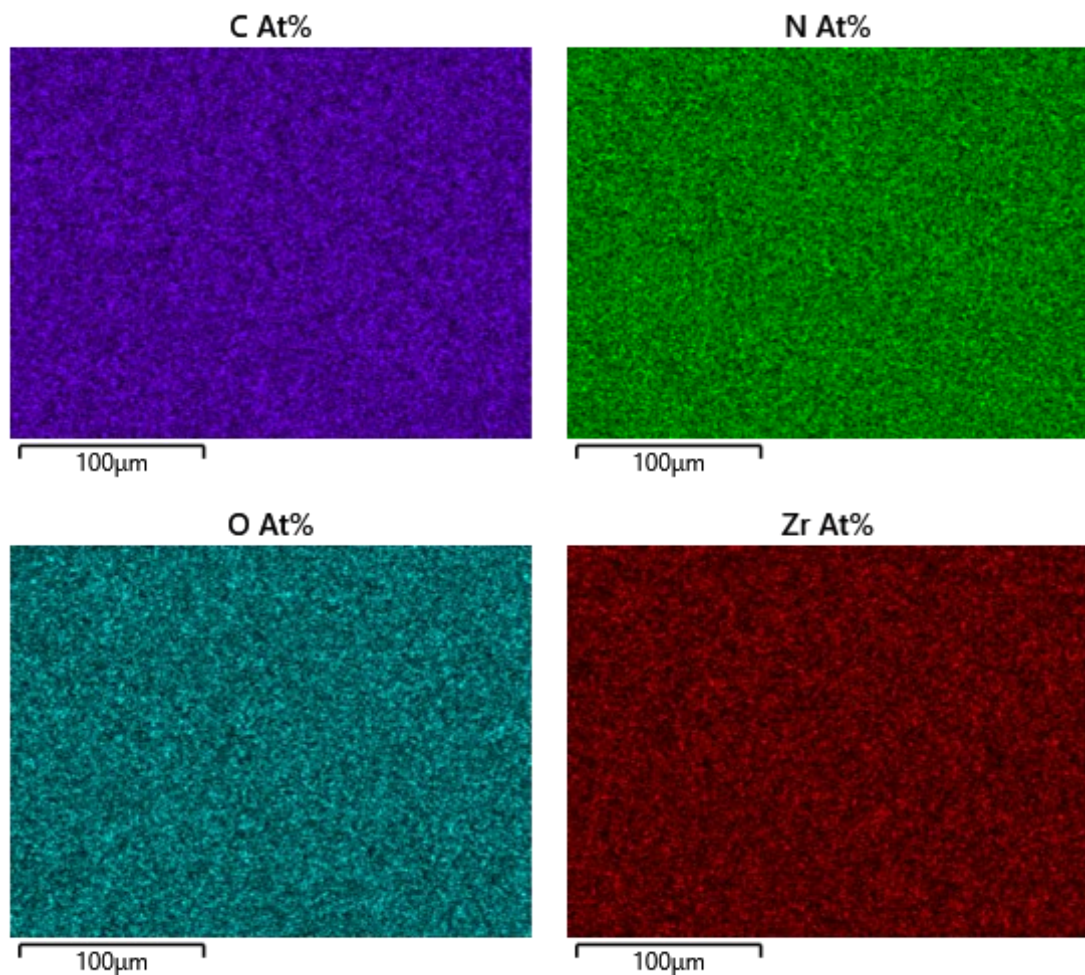


Fig S15. EDX maps of carbon (C), nitrogen (N), oxygen (O), and zirconium (Zr) from UiO-67-NH₂.

Table S7. EDX map results in atomic %, of UiO-67-NH₂.

Statistic	C (at %)	N (at %)	O (at %)	Zr (at %)
Max	68.37	4.10	22.55	4.98
Min	68.37	4.10	22.55	4.98
Average	68.37	4.10	22.55	4.98
Standard Deviation	0.00	0.00	0.00	0.00

S 9.3. EDX maps of UiO-67-2F

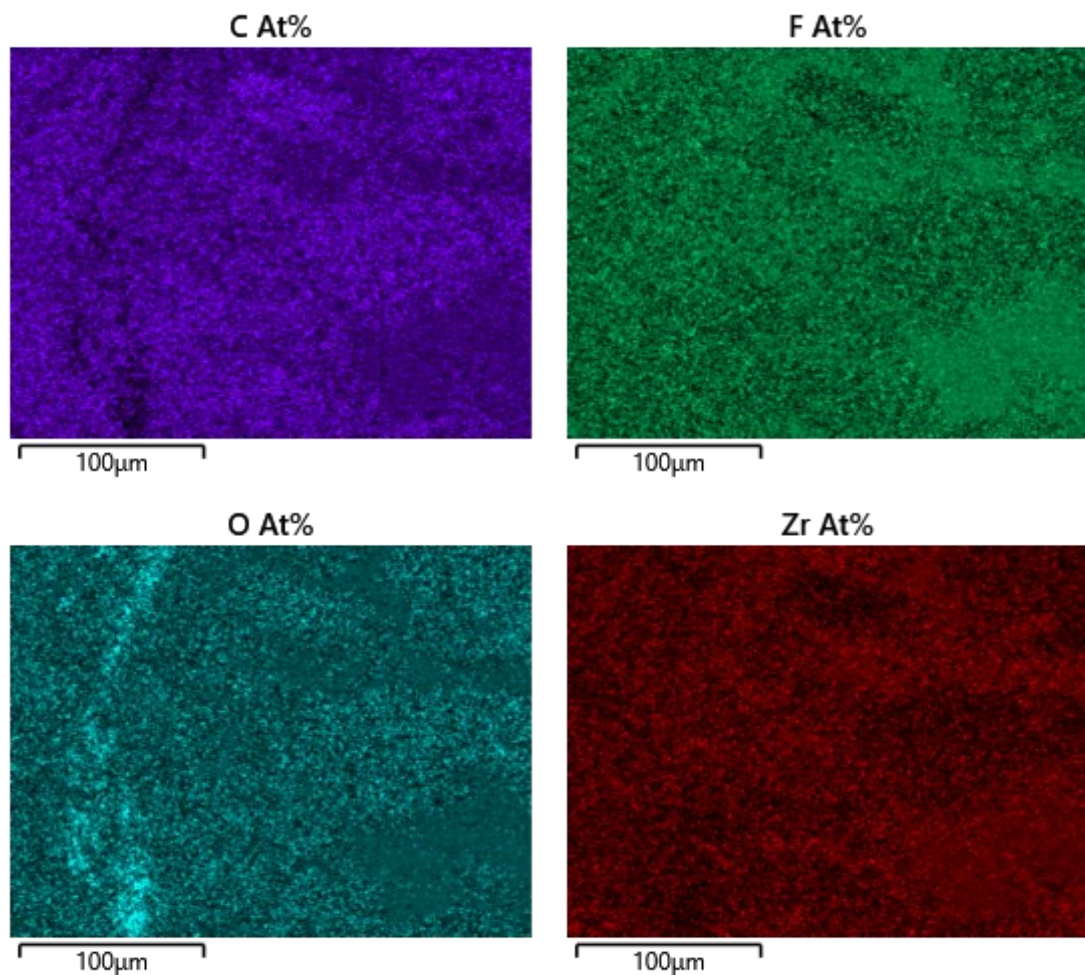


Fig S16. EDX maps of carbon (C), fluorine (F), oxygen (O), and zirconium (Zr) from UiO-67-2F.

Table S8. EDX map results in atomic %, of UiO-67-2F.

Statistic	C (at %)	O (at %)	F (at %)	Zr (at %)
Max	67.07	23.51	5.52	3.90
Min	67.07	23.51	5.52	3.90
Average	67.07	23.51	5.52	3.90
Standard Deviation	0.00	0.00	0.00	0.00

S 9.4. EDX maps of UiO-68-(CF₃)₂

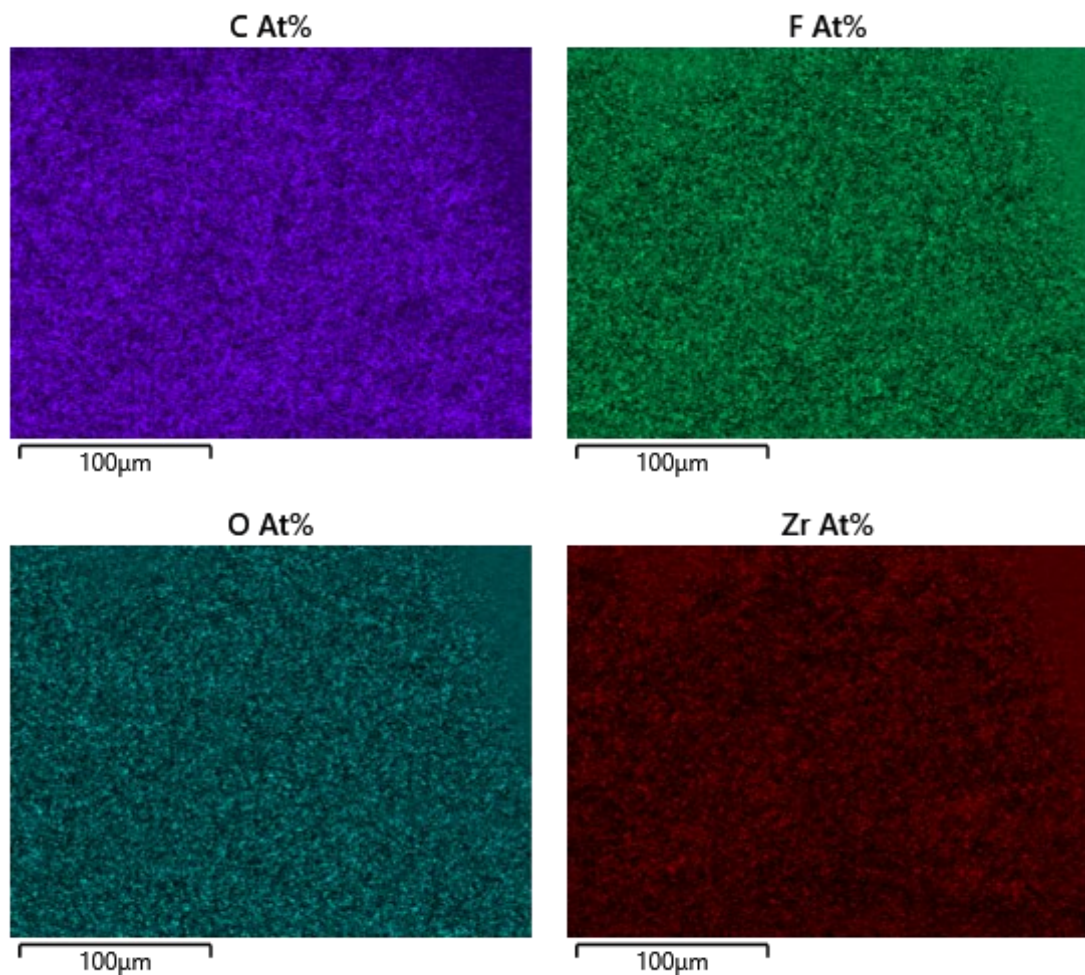


Fig S17. EDX maps of carbon (C), fluorine (F), oxygen (O), and zirconium (Zr) from UiO-68-(CF₃)₂.

Table S9. EDX map results in atomic %, of UiO-68-(CF₃)₂.

Statistic	C (at %)	O (at %)	F (at %)	Zr (at %)
Max	71.28	29.55	11.00	2.51
Min	67.94	15.72	11.00	2.01
Average	69.61	22.63	11.00	2.26
Standard Deviation	2.36	9.78	0.00	0.35

S 10. Scanning Transmission electron microscopy (STEM)

STEM images were collected on a FEI Titan Themis 200 transmission electron microscope (ThermoFisher, MA, USA) with a 200 kV XFEG, and super EDX-detectors.

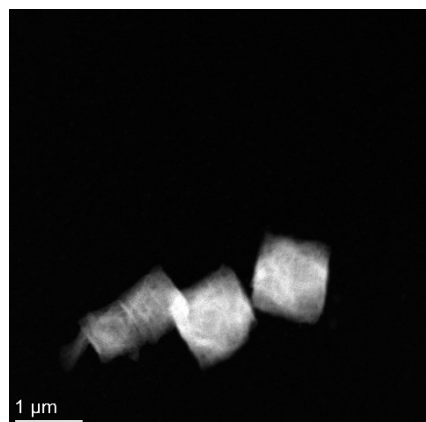


Fig S18. STEM HAADF image of UiO-76-F2.

S 10.1 Energy dispersive X-Ray spectroscopy (STEM-EDX)

STEM-EDX was performed on a FEI Titan Themis 200 transmission electron microscope (ThermoFisher, MA, USA), with a 200 kV XFEG, and super EDX-detectors.

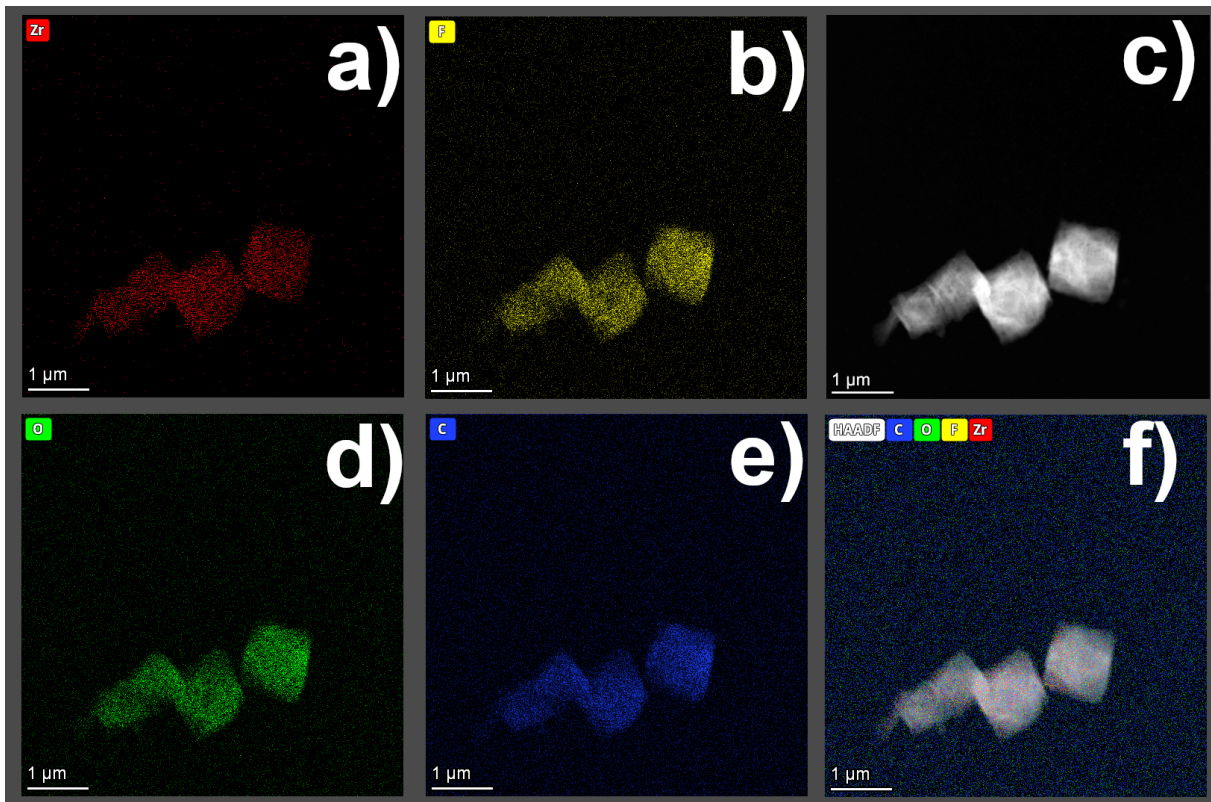


Fig S19. a) EDX zirconium (Zr) map b) EDX fluorine (F) map c) STEM HAADF image of UiO-76-F2. 200 kV acceleration voltage. d) EDX oxygen (O) map e) EDX carbon (C) map f) EDX combined elements/HAADF map

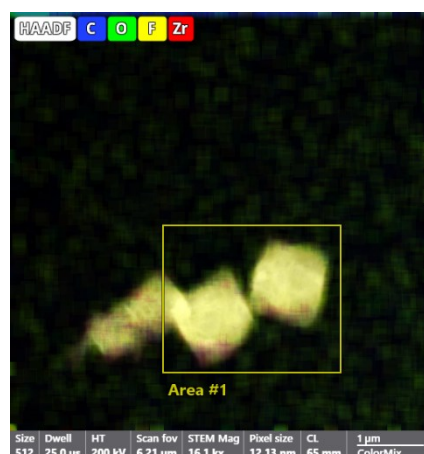


Fig S20. EDX combined elements/HAADF map of UiO-67-F2.

Table S10. Elemental composition obtained from STEM-EDX maps of UiO-67-F2.

Analysis of spectrum: Spectra from Area #1					
Z	Element	Family	Atomic Fraction (%)	Atomic Error (%)	Mass Fraction (%)
6	C	K	57.18	2.44	19.97
8	O	K	11.42	2.07	5.31
9	F	K	4.08	0.81	2.25
40	Zr	K	27.32	2.63	72.47

S 11. Transmission electron microscopy (TEM)

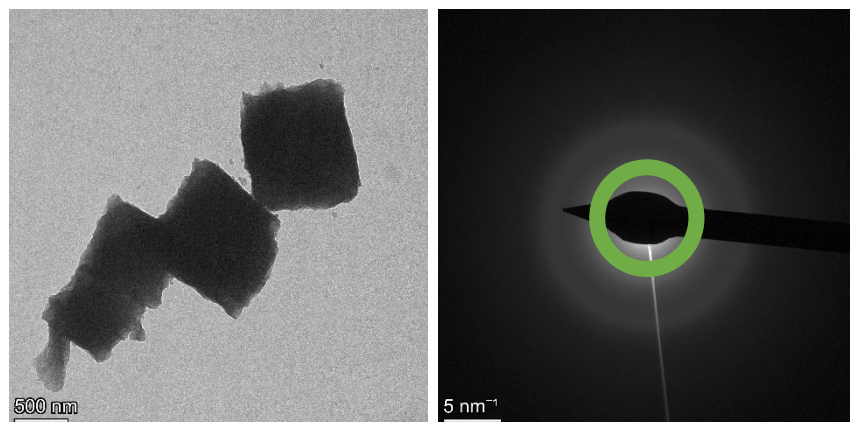


Fig S21. (Left) Brightfield (BF) TEM image taken at 200 kV acceleration voltage and (Right) selected area electron diffraction (SAED) patterns of UiO-67-2F. Note amorphous state of crystals which was obtained due to beam damage.

S 12. Gas sorption

Nitrogen sorption isotherms were recorded at -196 °C in a liquid nitrogen (N_2) bath on an Accelerated surface area and porosity (ASAP) 2020 (Micromeritics Instrument Corporation 4356 Communications Drive Norcross, GA 30093). Density functional theory (DFT) pore size distributions were calculated from the adsorption branch of the N_2 isotherms using the Micromeritics MicroActive software package (v.5.01), using a slit geometry kernel, and the N_2 -DFT model (with no regularization). Brunauer-Emmet-Teller (BET) specific surface areas (SSAs) were calculated from the adsorption branch using the BET Surface Identification (BETSI) software⁶ and Langmuir SSAs were calculated using the Micromeritics MicroActive software package in the p/p° ranges of 4.5–16.1 kPa (UiO-67-F2), 4.5–15.7 kPa (UiO-67-NH₂), 4.5–15 kPa (UiO-68-(CF₃)₃). N_2 , CH_4 , SF_6 and CO_2 gas sorption isotherms were measured at 0 – 20 °C using an insulating water/ice water bath.

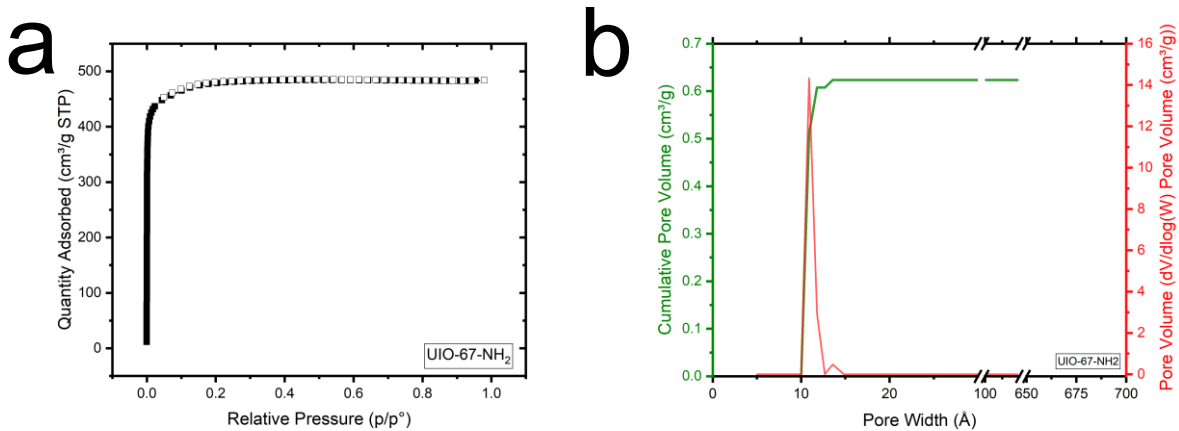


Fig S22. (a) N_2 sorption isotherm captured at -196 °C and (b) cumulative pore volume and DFT pore distribution of UIO-67-NH₂. Filled and hollow circles in the isotherm represent the adsorption and desorption branches, respectively.

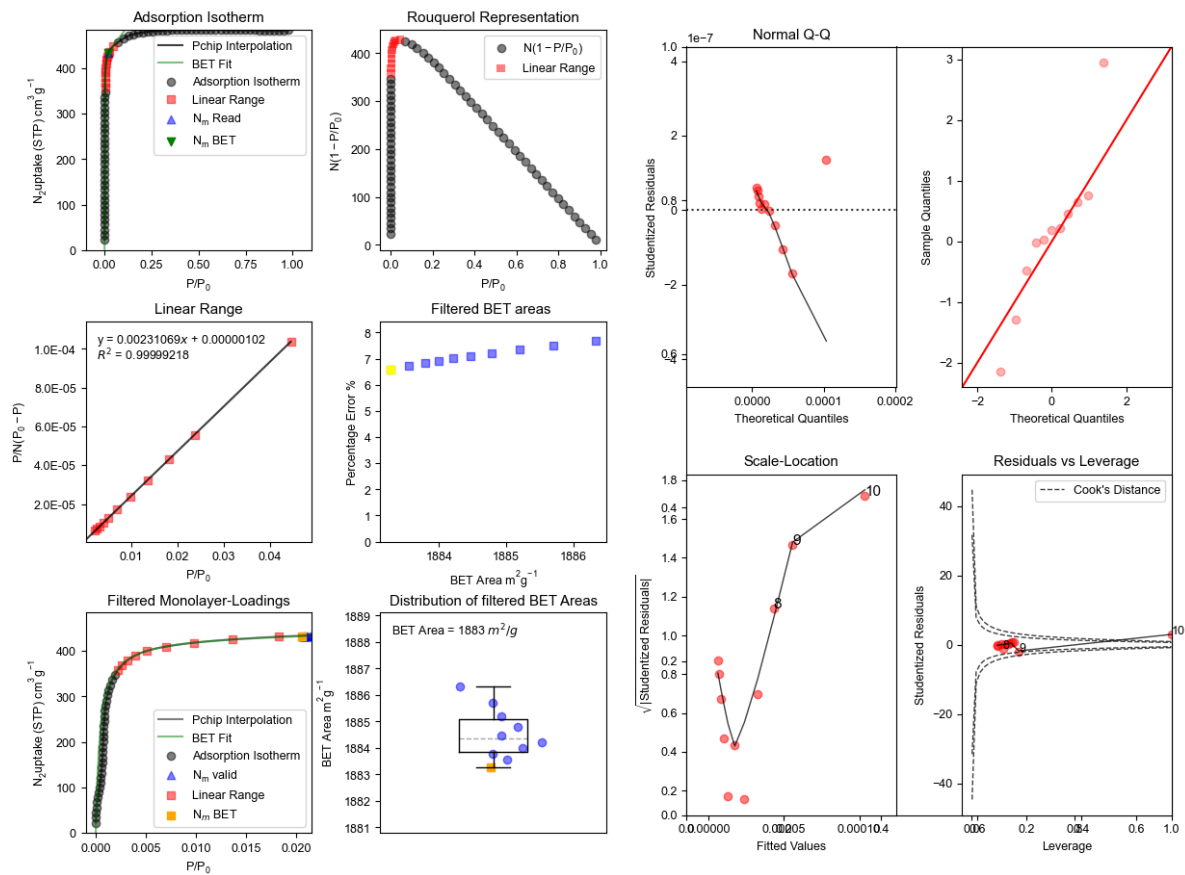


Fig S23. BETSI printouts for the BET fit of UIO-67-NH₂.

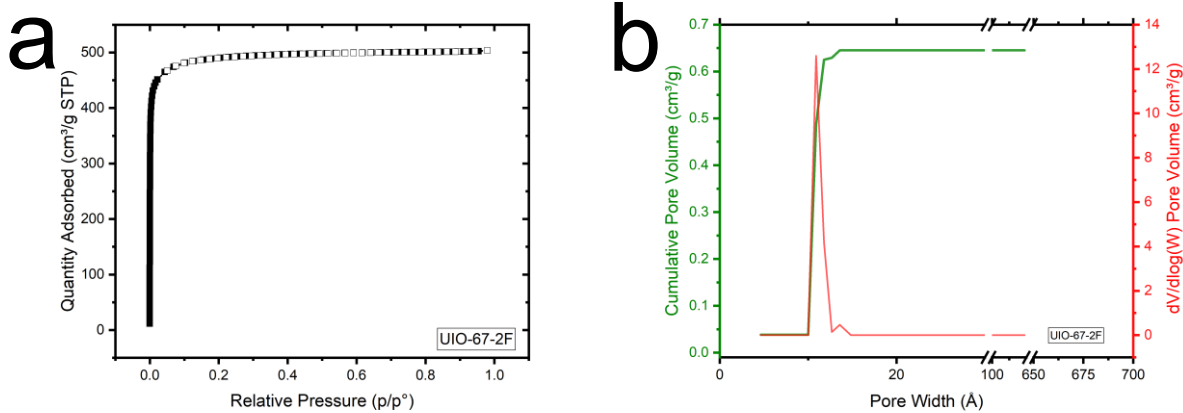


Fig S24. (a) N_2 sorption isotherm captured at $-196\text{ }^\circ\text{C}$ and (b) cumulative pore volume and DFT pore distribution of UIO-67-F2. Filled and hollow circles in the isotherm represent the adsorption and desorption branches, respectively.

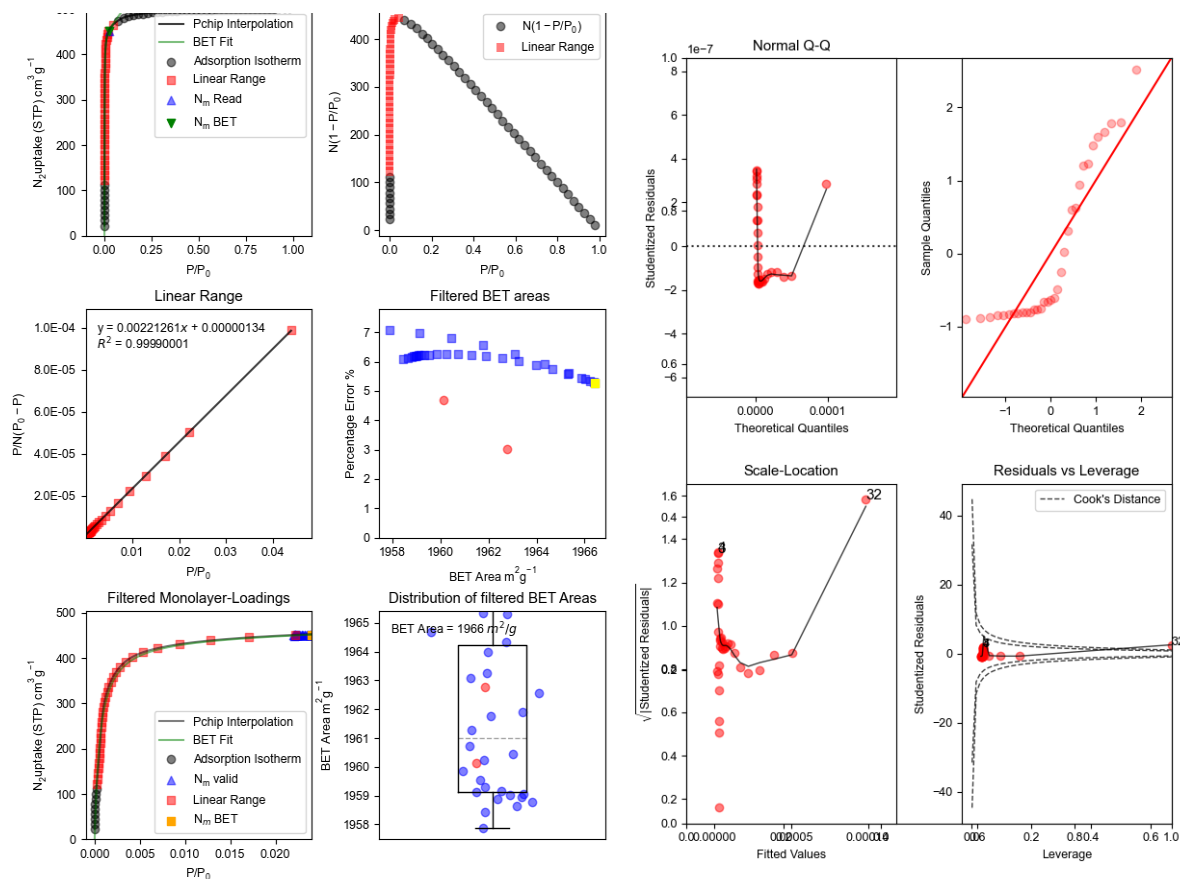


Fig S25. BETSI printouts for the BET fit of UIO-67-F2.

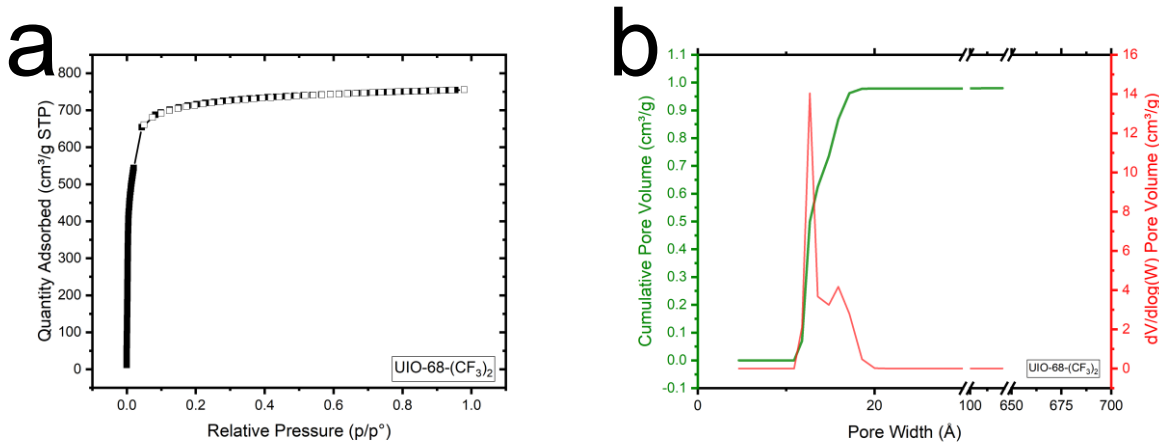


Fig S26. (a) N_2 sorption isotherm captured at $-196\text{ }^\circ\text{C}$ and (b) cumulative pore volume and DFT pore distribution of $\text{UIO-68-(CF}_3)_2$. Filled and hollow circles in the isotherm represent the adsorption and desorption branches, respectively.

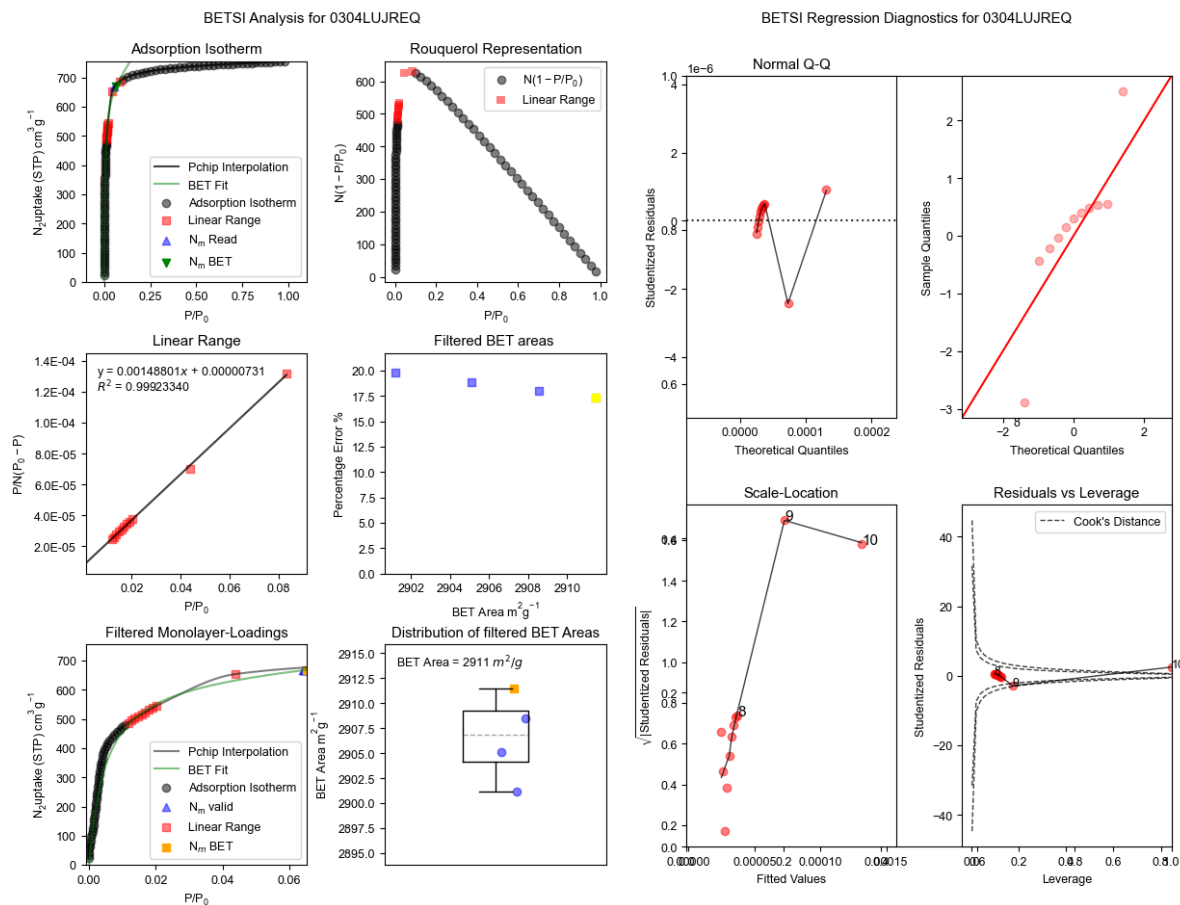


Fig S27. BETSI printouts for the BET fit of $\text{UIO-68-(CF}_3)_2$.

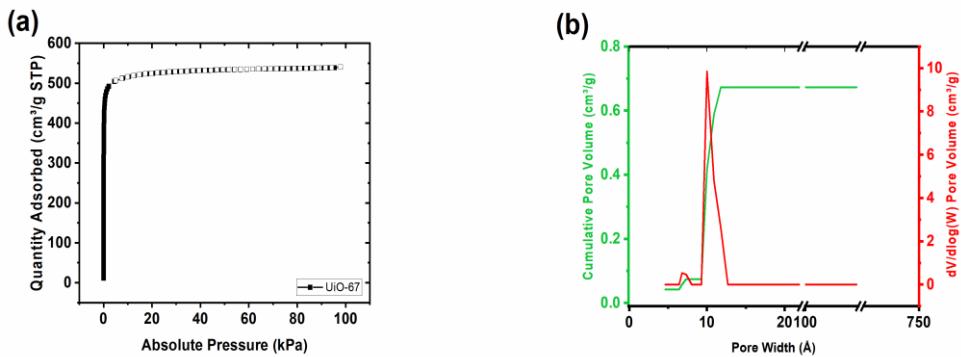


Fig S28. (a) N₂ sorption isotherm captured at -196 °C and (b) cumulative pore volume and DFT pore distribution of UIO-67. Filled and hollow circles in the isotherm represent the adsorption and desorption branches, respectively.

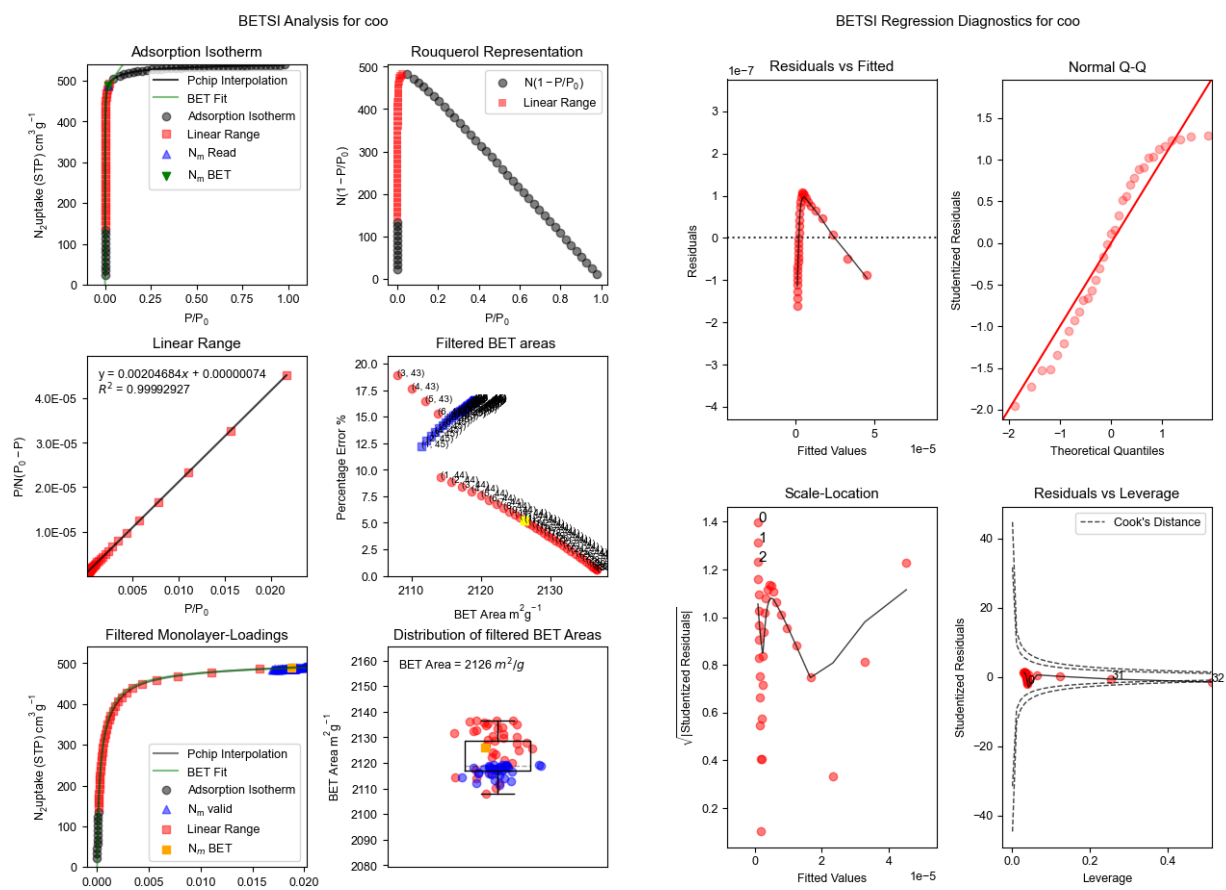


Fig S29. BETSI printouts for the BET fit of UIO-68-(CF3)2.

Table S11. Brunauer-Emmett-Teller (BET) and Langmuir specific surface areas (SSAs), total pore volumes, and pore sizes of UiO-67 and -68 analogues.

Sample	SSA_{BET}^a (m ² /g)	V_{tot}^b (cm ³ /g)	Pore size (Å)
UiO-67	2126	0.838	10.0
UiO-67-F2	1966	0.781	10.9, 13.5
UiO-67-NH ₂	1883	0.750	10.9, 13.5
UiO-68-(CF ₃) ₂	2911	1.170	12.7, 15.7

^aCalculated from N₂ adsorption isotherms recorded at -196 °C using the BETSI software,

^bEstimated from N₂ adsorption isotherms recorded at -196 °C at p/p° = 0.99.

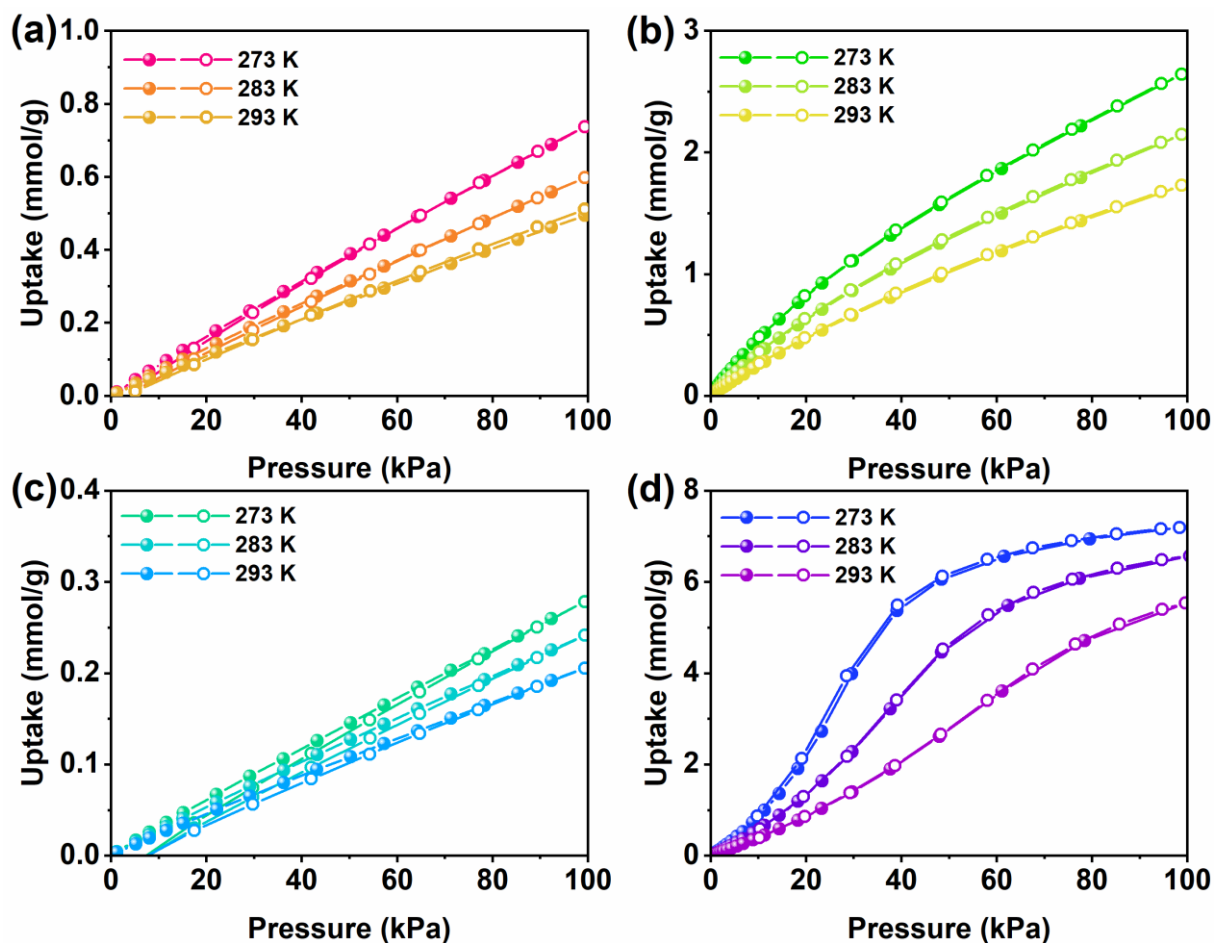


Fig S30. Gas sorption isotherms recorded at 0 – 20 °C of (a) CH₄, (b) CO₂, (c) N₂, and (d) SF₆ for UiO-67-NH₂. Filled markers represent adsorption points, hollow represent desorption branch. The interconnecting line is intended to guide the eye.

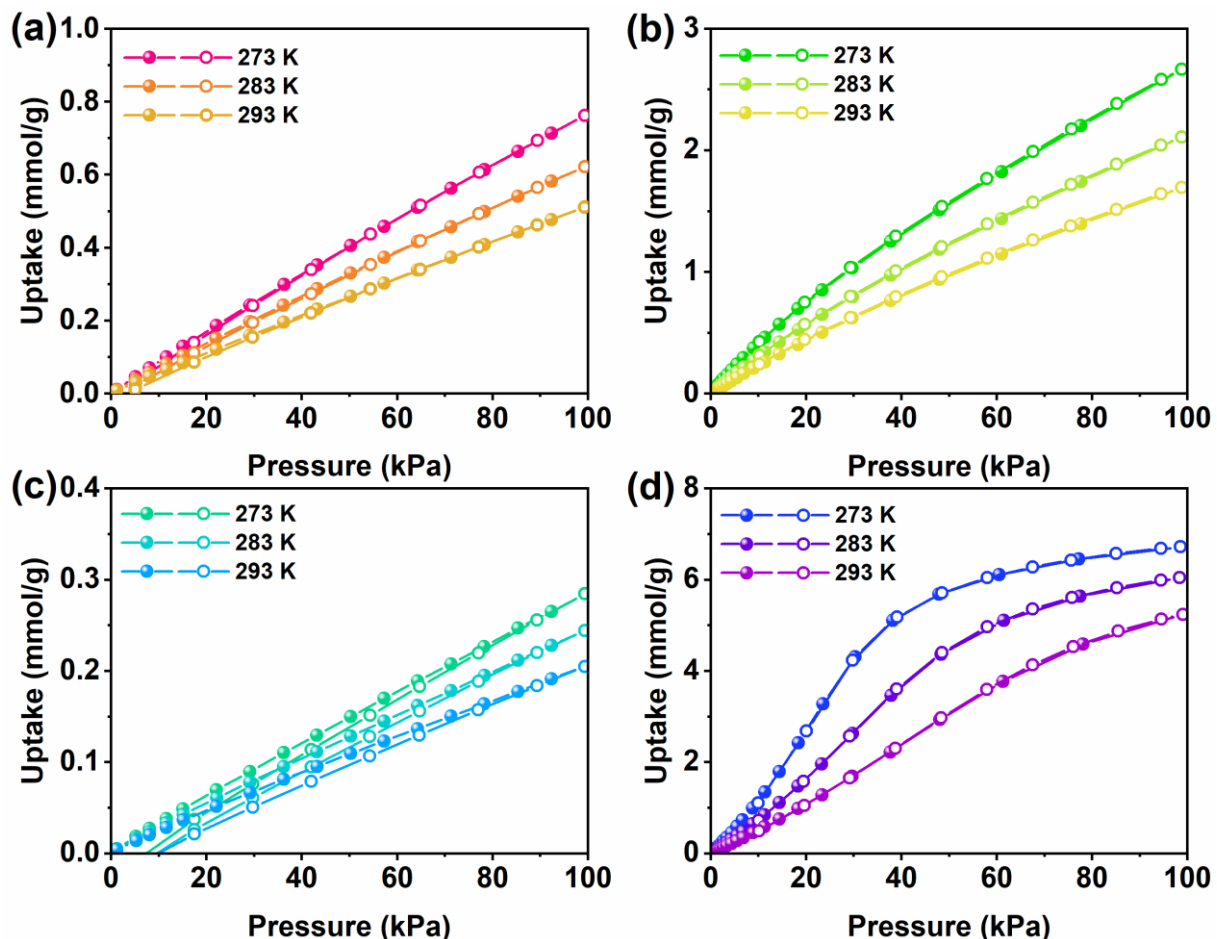


Fig S31. Gas sorption isotherms recorded at 0 – 20 °C of (a) CH_4 , (b) CO_2 , (c) N_2 , and (d) SF_6 for UiO-67-F2. Filled markers represent adsorption points, hollow represent desorption branch. The interconnecting line is intended to guide the eye.

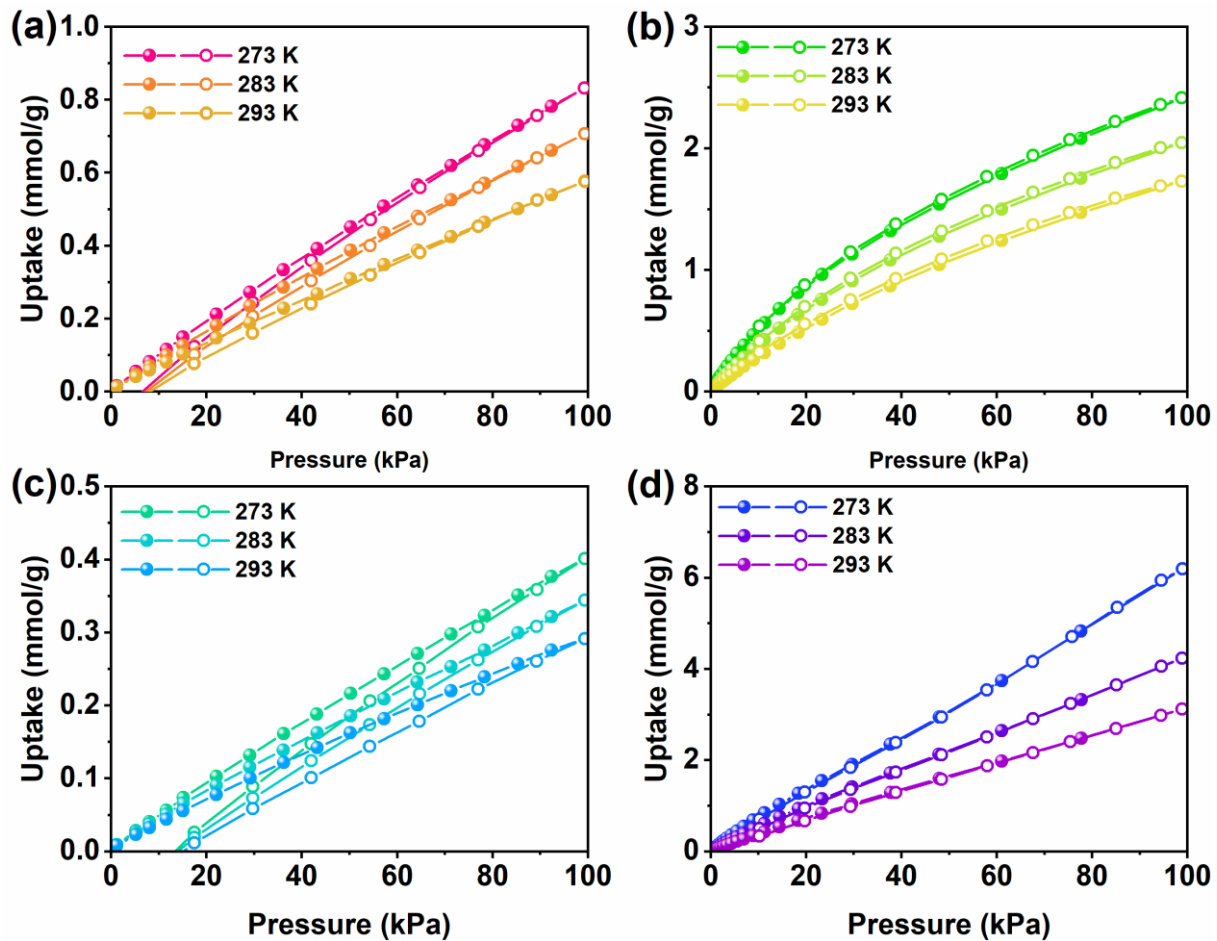


Fig S32. Gas sorption isotherms recorded at 0 – 20 °C of (a) CH₄, (b) CO₂, (c) N₂, and (d) SF₆ for UiO-68-(CF₃)₂. Filled markers represent adsorption points, hollow represent desorption branch. The interconnecting line is intended to guide the eye.

Table S12. Summary of CH₄, CO₂, N₂, and SF₆ uptake at 0 – 20 °C and 100 kPa.

Temperature (°C)	CH ₄ (mmol/g)	CO ₂ (mmol/g)	N ₂ (mmol/g)	SF ₆ (mmol/g)
UiO-67-F2				
0	0.76	2.67	0.28	6.72
10	0.62	2.11	0.24	6.05
20	0.51	1.69	0.21	5.24
UiO-67-NH2				
0	0.74	2.64	0.28	7.20
10	0.60	2.15	0.24	6.58
20	0.49	1.73	0.21	5.54
UiO-68-(CF₃)₂				
0	0.83	2.42	0.40	6.20
10	0.71	2.05	0.34	4.24
20	0.58	1.73	0.29	3.12

S 13. Isosteric enthalpy of adsorption

Isosteric enthalpies of adsorption was calculated by the Clausius Clapeyron method. The uptake represented in the calculations were present in the captured isotherms. Means and mean errors were calculated across a total of 50 points, where the standard errors are reduced chi squared-scaled standard error from the linear fit of the isosteres.

The following is a short reasoning summary of the chemical thermodynamics behind this method, the background was added to demonstrate that changing the examined units from mmol/g to mmol/SSA does not change or contradict the underlying theory.

These isotherms were then fit to a dual-site-Langmuir isotherm function, which was used to create continuity at all points of the isotherms.

A span of uptakes present at all three temperatures is chosen as range to be examined (lowest uptake of the low temperature, to the highest point of the highest temperature), and the logarithm of the pressures $\ln(P)$ present in this range is, transposed and plotted vs $1/T$.

This should in theory create linear isosteres, where the $[\ln(kPa)]$ of each is dependent on temperature (K) only. The differential of these isosteres is multiplied with the general gas constant and adjusted to yield the differential enthalpy of adsorption (kJ/mol) (ΔH_{ads}). Any deviation from linearity here is measured as a standard error in the fit.

The background of the isosteric heat of adsorption can be found in several sources, few of which explain the thermodynamical background in any depth. A slightly more in-depth description can be the following⁷;

The Helmholtz free energy, F , for a system in equilibrium at a specific uptake n is given by **Eq. 1**,

$$F^\sigma = F - F^g - F^s \quad \text{Eq. 1}$$

with g - gaseous adsorptive, and s - solid adsorbent.

As uptake does not change at equilibrium, the change in surface excess amount (n) is given by **Eq. 2**.

$$\delta n = \delta n^\sigma + \delta n^g = 0 \rightarrow \delta n^\sigma = -\delta n^g \quad \text{Eq. 2}$$

In turn, **Eq. 1** and **Eq. 2** can be rearranged into,

$$\left(\frac{\delta F^\sigma}{\delta n^\sigma}\right)_{T,A} = -\left(\frac{\delta F^g}{\delta n^\sigma}\right)_{T,V} = +\left(\frac{\delta F^\sigma}{\delta n^g}\right)_{T,V} \quad \text{Eq. 3}$$

where T , A , and V represent dependence on temperature, area, and volume, respectively. The index refers to these parameters being constant.

The chemical potential of the gas is,

$$\mu^g = \left(\frac{\delta F^g}{\delta n^\sigma}\right)_{T,V} \quad \text{Eq. 4}$$

Similarly, the chemical potential of the surface excess chemical potential is,

$$\mu^\sigma = \left(\frac{\delta F^\sigma}{\delta n^\sigma}\right)_{T,A} \quad \text{Eq. 5}$$

As equilibrium,

$$\mu^\sigma = \mu^g \quad \text{Eq. 6}$$

which means, the chemical potential of the adsorbate, is the same as the chemical potential of the adsorbate in the gas phase (the same temperature, area, and volume, **Eq. 4 – 6**).

The differential, surface excess internal energy can be written,

$$\dot{u}_{T,\theta}^\sigma = \left(\frac{\delta U^\sigma}{\delta n^\sigma} \right)_{T,A} \quad \text{Eq. 7}$$

where θ is the surface excess concentration (commonly called the uptake, **Eq. 7**) and the differential surface excess entropy (**Eq. 8**), $\dot{S}_{T,\theta}^\sigma$, as

$$\dot{S}_{T,\theta}^\sigma = \left(\frac{\delta S^\sigma}{\delta n^\sigma} \right)_{T,A} \quad \text{Eq. 8}$$

Under the prerequisites that T , V , and A are held constant, and the gas behaving ideally; which is true of a system pertaining one material species at equilibrium, $\mu^\sigma = \mu^g$, can be re-written,

$$\dot{u}_{T,\theta}^\sigma - T\dot{S}_{T,\theta}^\sigma = u_T^g + RT - TS_{T,P}^g \quad \text{Eq. 9}$$

Additionally,

$$S_{T,P}^g = S_T^{g,\emptyset} - R * \ln\left(\frac{p}{P^\emptyset}\right) \quad \text{Eq. 10}$$

where $S_T^{g,\emptyset}$ is the molar standard entropy of the ideal gaseous adsorptive at T and P^\emptyset is 105 Pa (this term, $\frac{p}{P^\emptyset}$, is commonly just mentioned as p/p° and is in no way related to the saturation pressure. P^\emptyset is the immersion vapour pressure at the set temperature).

These last two equations can be rearranged into (**Eq. 11**)

$$\ln\left(\frac{p}{P^\emptyset}\right) = \frac{\dot{u}_{T,\theta}^\sigma - u_T^g - RT}{RT} - \frac{\dot{S}_{T,\theta}^\sigma - S_T^{g,\emptyset}}{R} \quad \text{Eq. 11}$$

A subtle reminder here is that central dots convey the mathematical notation that it is the derivative.

This equation, is differentiated dT , so that the surface excess concentration θ remains constant, and assume that $\Delta_{ads}\dot{h}_{T,\theta}$ and $\Delta_{ads}\dot{S}_{T,\theta}$ do not vary **Eq. 11** can be written,

$$\left(\frac{d}{dT} \ln(P) \right)_\theta = - \frac{\Delta_{ads}\dot{h}_{T,\theta}}{RT^2} \quad \text{Eq. 12}$$

Which is rearranged into (often mentioned in literature) (**Eq. 13**),

$$-\Delta_{ads}\dot{h}_{T,\theta} = R \left(\frac{\ln(P)}{d_T^1} \right)_\theta \quad \text{Eq. 13}$$

The index in this case, refers to a certain uptake (meaning uptake is at equilibrium).

In addition to explaining how this method is derived, if the area (A), temperature (T), and volume (V) of the adsorptive remains unchanged during the assumed equilibrium, **Eq. 3**. holds true, which in turn means **Eq. 13** holds true.

This also shows that there is no need to use an isotherm-model which represents a specific physical process, for this method to work. We already have empirical data pertaining uptake, pressure, and temperature. The reason we need a model at all is to ensure that there are points present at the same surface concentration at a specific pressure on all involved

temperatures. This can easily be achieved by using a suitable mathematical model. The model is essentially connecting the discrete points of the isotherm, without over-parametrizing. As the empirical data itself clearly is a representation of a physical process, connecting its data points using a continuous function should not require some great consideration.

In addition, results presented include a standard error, which is calculated from the linear fit of Eq. 13 onto the discrete data points of $\ln(P)$ vs $1/T$.

S 13.1. Isosteric enthalpy of CO₂ adsorption

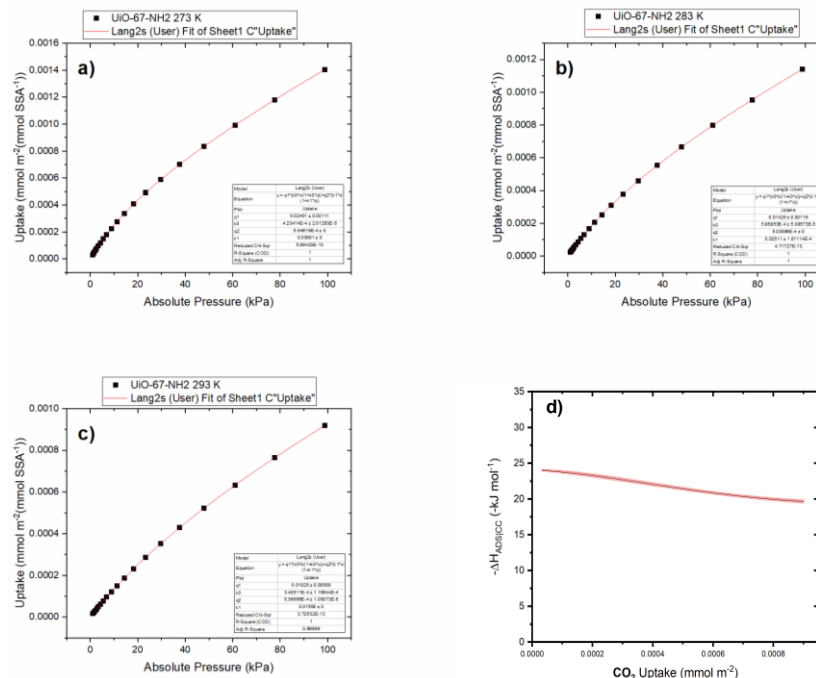


Fig S33. Adsorption isotherms of CO₂ onto UiO-67-NH₂ and dual-site Langmuir fits at a) 0 °C, b) 10 °C, c) 20 °C, and d) isosteric enthalpy CO₂ adsorption onto UiO-67-NH₂ as a function of mmol CO₂ per m² sorbent (normalized by the BET specific surface area of the MOF). The standard error of the fitted isosteres is represented by the red highlight.

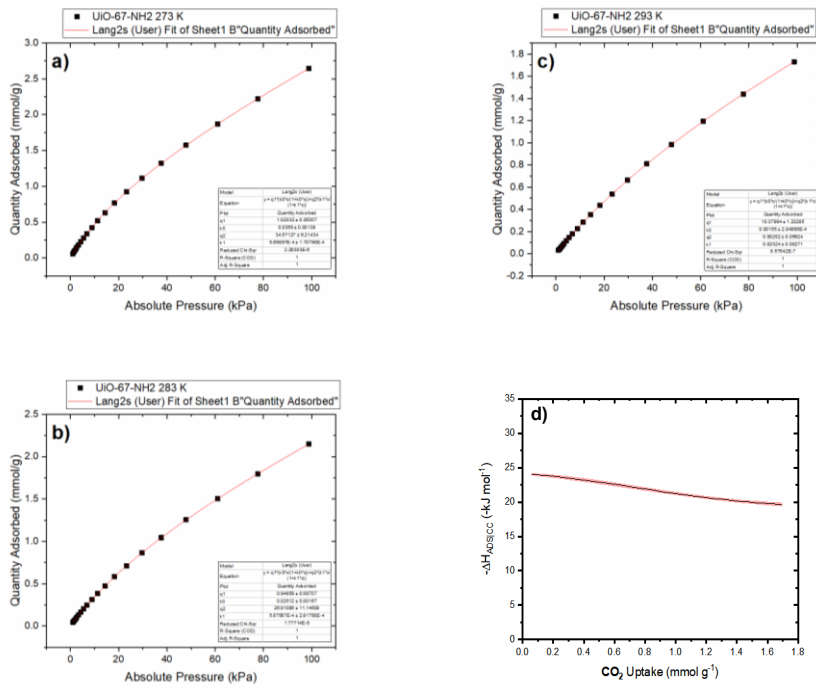


Fig S34. Adsorption isotherms of CO₂ onto UiO-67-NH₂ and dual-site Langmuir fits at a) 0 °C, b) 10 °C, c) 20 °C, and d) isosteric enthalpy CO₂ adsorption onto UiO-67-NH₂ as a function of mmol CO₂ per g sorbent. The standard error of the fitted isosteres is represented by the red highlight.

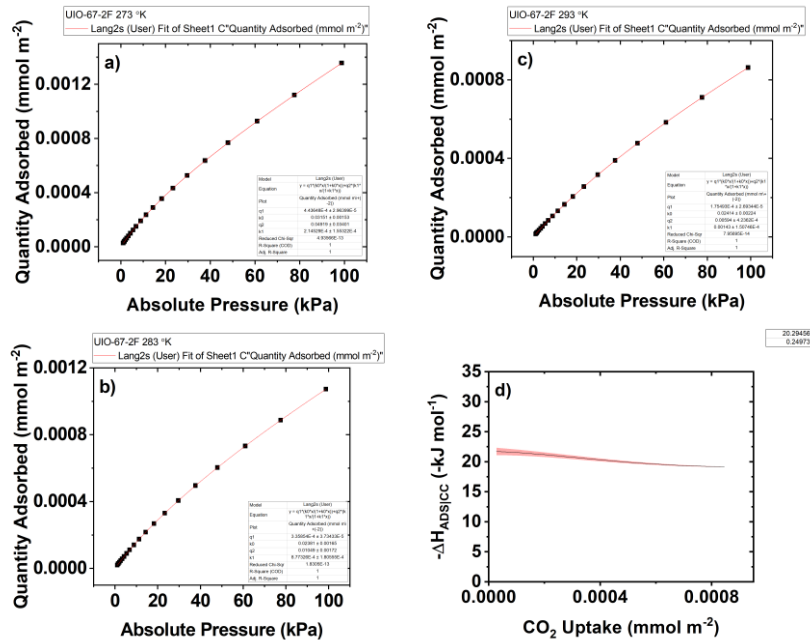


Fig S35. Adsorption isotherms of CO₂ onto UiO-67-F2 and dual-site Langmuir fits at a) 0 °C, b) 10 °C, c) 20 °C, and d) isosteric enthalpy CO₂ adsorption onto UiO-67-F2 as a function of mmol CO₂ per m² sorbent (normalized by the BET specific surface area of the MOF). The standard error of the fitted isosteres is represented by the red highlight.

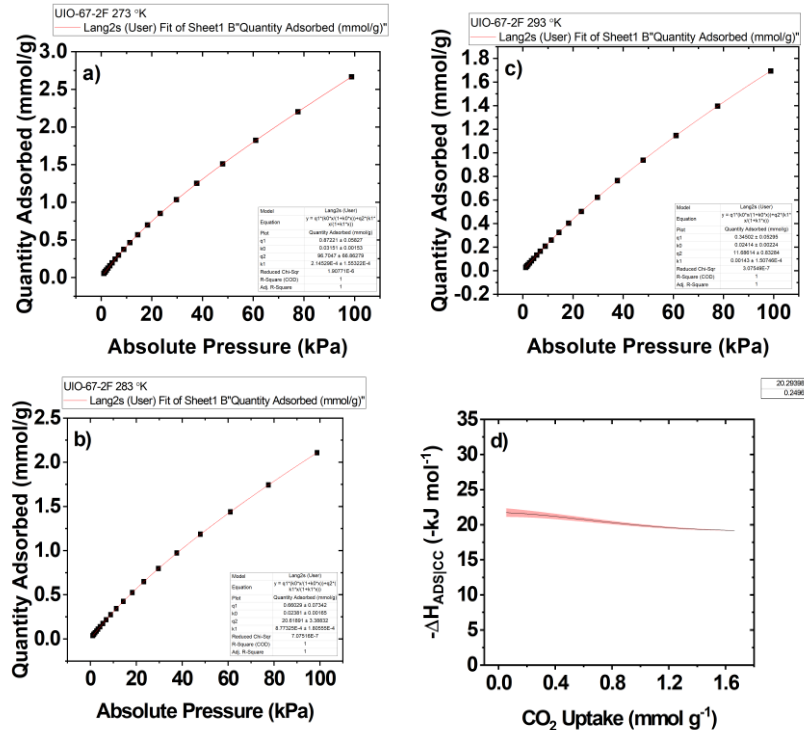


Fig S36. Adsorption isotherms of CO₂ onto UiO-67-F2 and dual-site Langmuir fits at a) 0 °C, b) 10 °C, c) 20 °C, and d) isosteric enthalpy CO₂ adsorption onto UiO-67-F2 as a function of mmol CO₂ per g sorbent. The standard error of the fitted isosteres is represented by the red highlight.

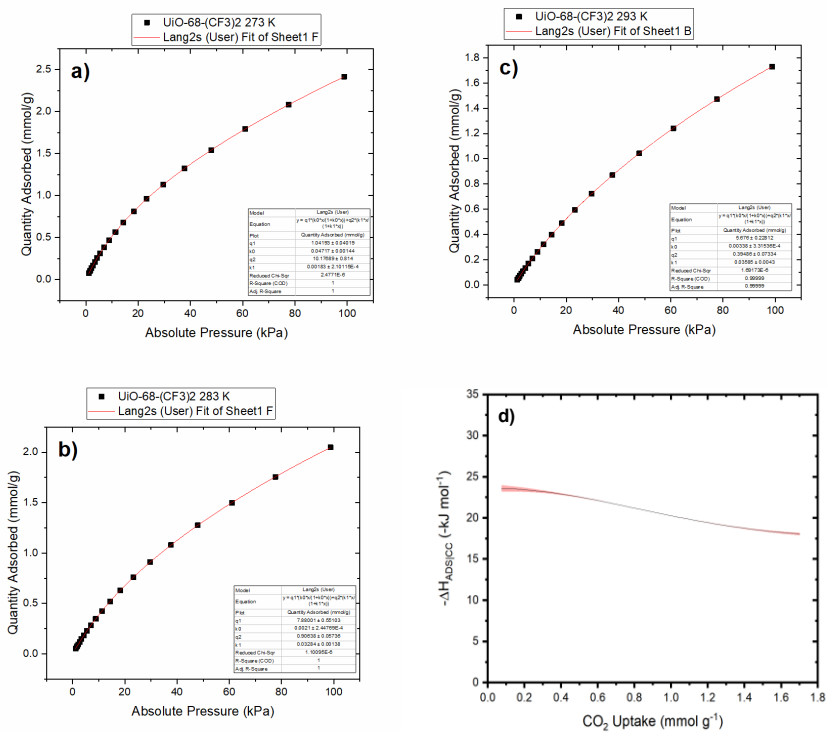


Fig S37. Adsorption isotherms of CO₂ onto UiO-68-(CF3)2 and dual-site Langmuir fits at a) 0 °C, b) 10 °C, c) 20 °C, and d) isosteric enthalpy CO₂ adsorption onto UiO-68-(CF3)2 as a function of mmol CO₂ per g sorbent. The standard error of the fitted isosteres is represented by the red highlight.

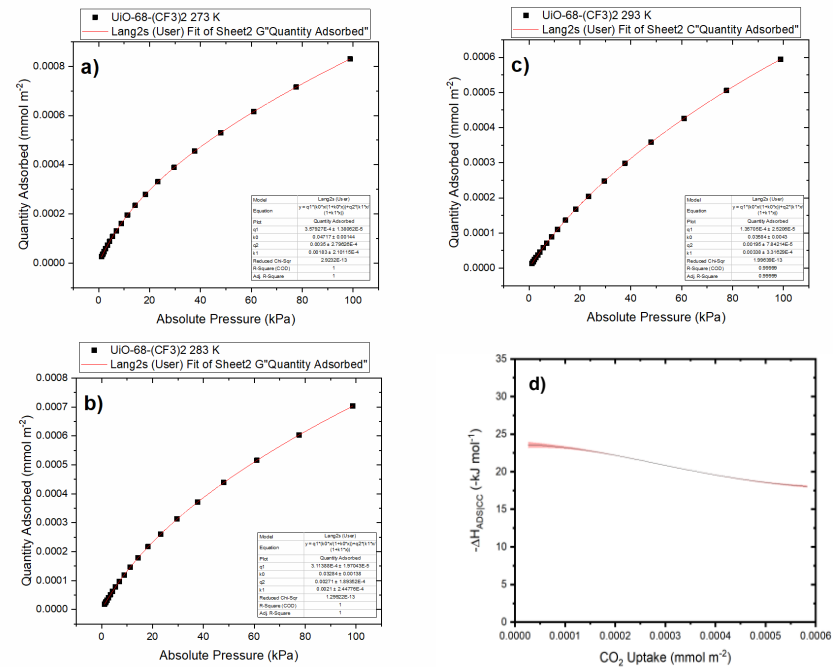


Fig S38. Adsorption isotherms of CO₂ onto UiO-68-(CF3)2 and dual-site Langmuir fits at a) 0 °C, b) 10 °C, c) 20 °C, and d) isosteric enthalpy CO₂ adsorption onto UiO-68-(CF3)2 as a

function of mmol CO₂ per m² sorbent (normalized by the BET specific surface area of the MOF). The standard error of the fitted isosteres is represented by the red highlight.

S 13.2. Isosteric enthalpy of CH₄ adsorption

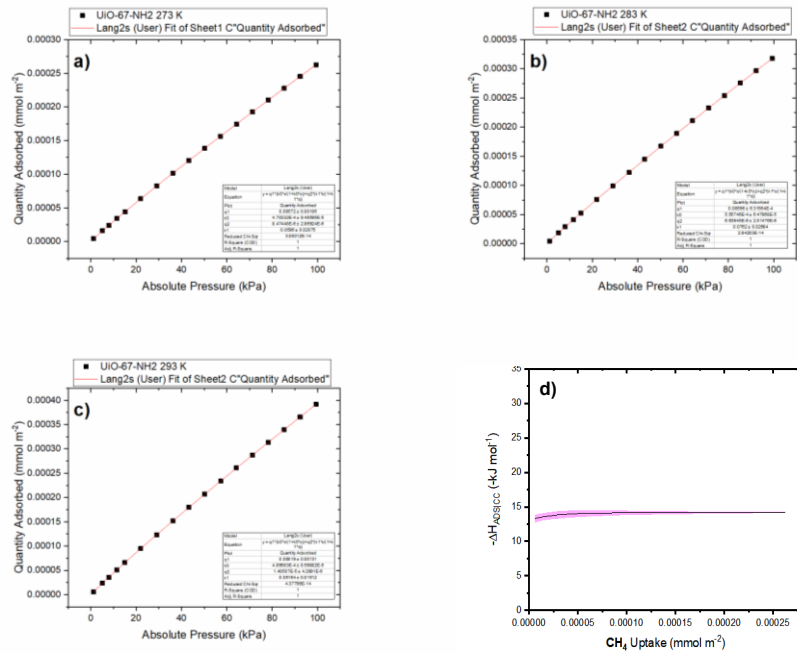


Fig S39. Adsorption isotherms of CH₄ onto UiO-67-NH2 and dual-site Langmuir fits at a) 0 °C, b) 10 °C, c) 20 °C, and d) isosteric enthalpy CO₂ adsorption onto UiO-67-NH2 as a function of mmol CH₄ per m² sorbent (normalized by the BET specific surface area of the MOF). The standard error of the fitted isosteres is represented by the magenta highlight.

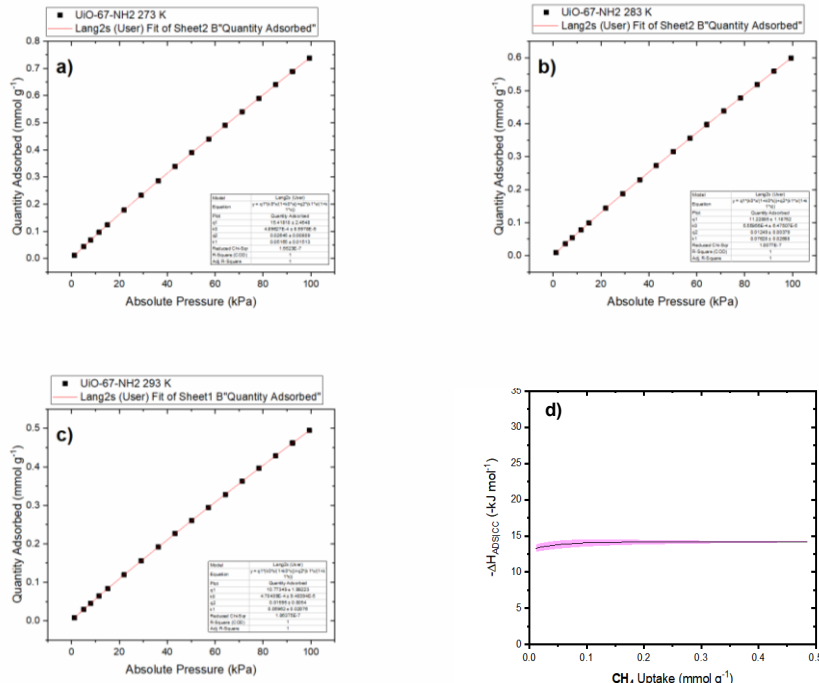


Fig S40. Adsorption isotherms of CH₄ onto UiO-67-NH2 and dual-site Langmuir fits at a) 0 °C, b) 10 °C, c) 20 °C, and d) isosteric enthalpy CO₂ adsorption onto UiO-67-NH2 as a function of

mmol CH₄ per g sorbent. The standard error of the fitted isosteres is represented by the magenta highlight.

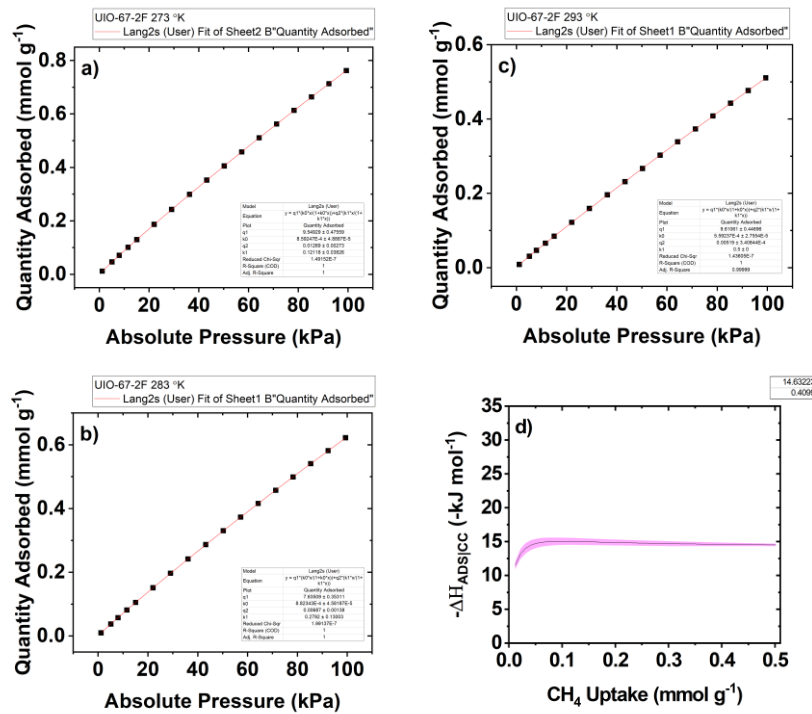


Fig S41. Adsorption isotherms of CH₄ onto UiO-67-F2 and dual-site Langmuir fits at a) 0 °C, b) 10 °C, c) 20 °C, and d) isosteric enthalpy CO₂ adsorption onto UiO-67-F2 as a function of mmol CH₄ per g sorbent. The standard error of the fitted isosteres is represented by the magenta highlight.

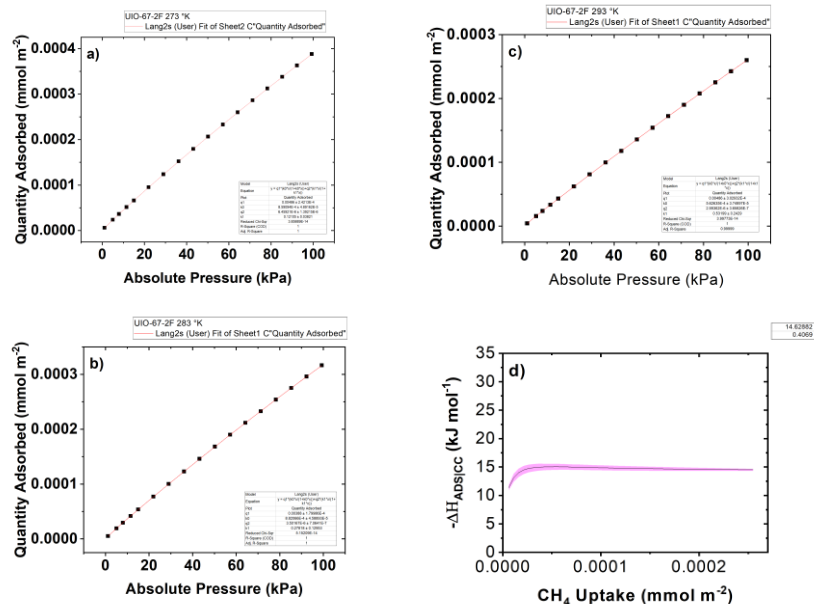


Fig S42. Adsorption isotherms of CH₄ onto UiO-67-F2 and dual-site Langmuir fits at a) 0 °C, b) 10 °C, c) 20 °C, and d) isosteric enthalpy CO₂ adsorption onto UiO-67-F2 as a function of mmol CH₄ per m² sorbent (normalized by the BET specific surface area of the MOF). The standard error of the fitted isosteres is represented by the magenta highlight

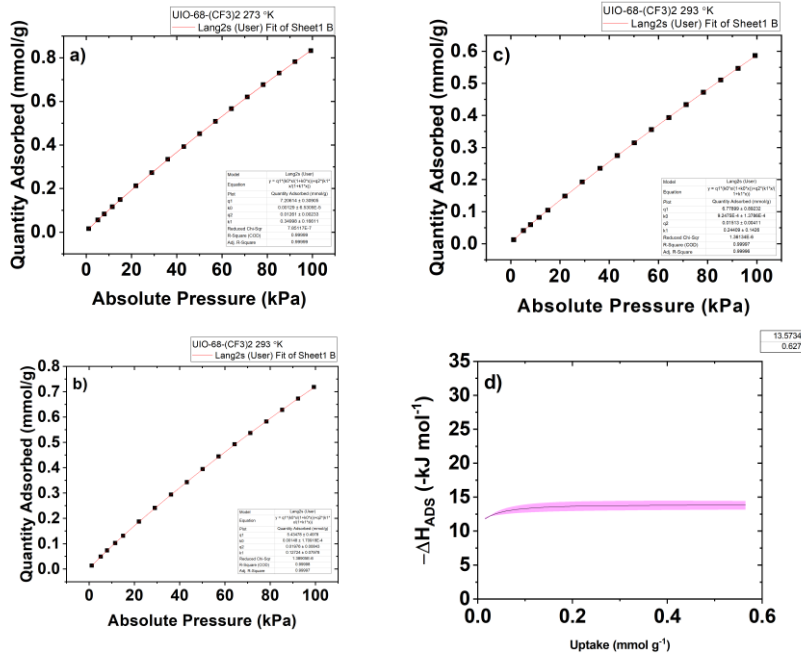


Fig S43. Adsorption isotherms of CH_4 onto UiO-68-(CF3)_2 and dual-site Langmuir fits at a) $0\text{ }^\circ\text{C}$, b) $10\text{ }^\circ\text{C}$, c) $20\text{ }^\circ\text{C}$, and d) isosteric enthalpy CO_2 adsorption onto UiO-68-(CF3)_2 as a function of mmol CH_4 per g sorbent. The standard error of the fitted isosteres is represented by the magenta highlight.

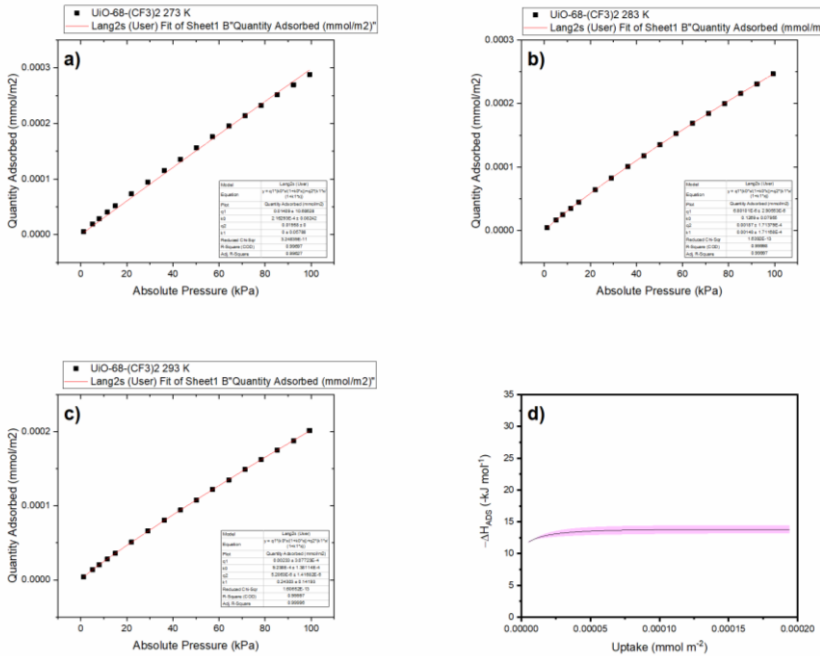


Fig S44. Adsorption isotherms of CH_4 onto UiO-68-(CF3)_2 and dual-site Langmuir fits at a) $0\text{ }^\circ\text{C}$, b) $10\text{ }^\circ\text{C}$, c) $20\text{ }^\circ\text{C}$, and d) isosteric enthalpy CO_2 adsorption onto UiO-68-(CF3)_2 as a function of mmol CH_4 per m 2 sorbent (normalized by the BET specific surface area of the MOF). The standard error of the fitted isosteres is represented by the magenta highlight

S 13.3. Isosteric enthalpy of SF₆ adsorption

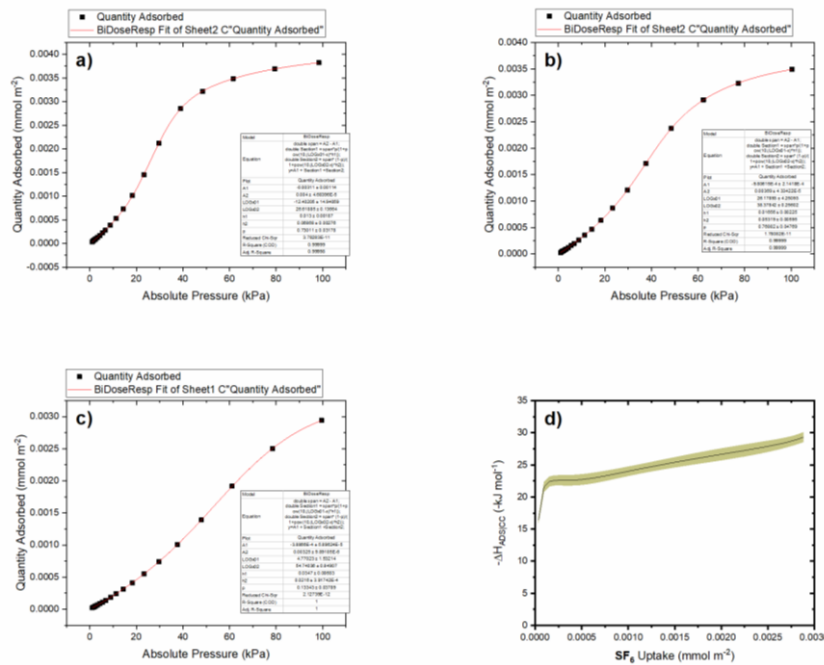


Fig S45. Adsorption isotherms of SF₆ onto UiO-67-NH₂ and fits at a) 0 °C, b) 10 °C, c) 20 °C, and d) isosteric enthalpy SF₆ adsorption onto UiO-67-NH₂ as a function of mmol SF₆ per m² sorbent (normalized by the BET specific surface area of the MOF). The standard error of the fitted isosteres is represented by the brown highlight

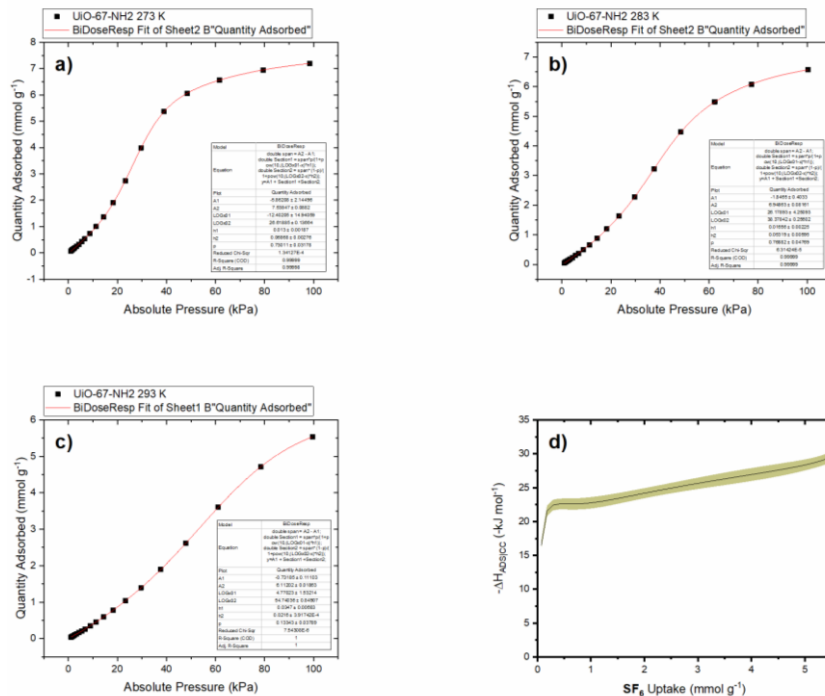


Fig S46. Adsorption isotherms of SF₆ onto UiO-67-NH₂ and fits at a) 0 °C, b) 10 °C, c) 20 °C, and d) isosteric enthalpy SF₆ adsorption onto UiO-67-NH₂ as a function of mmol SF₆ per g sorbent. The standard error of the fitted isosteres is represented by the brown highlight

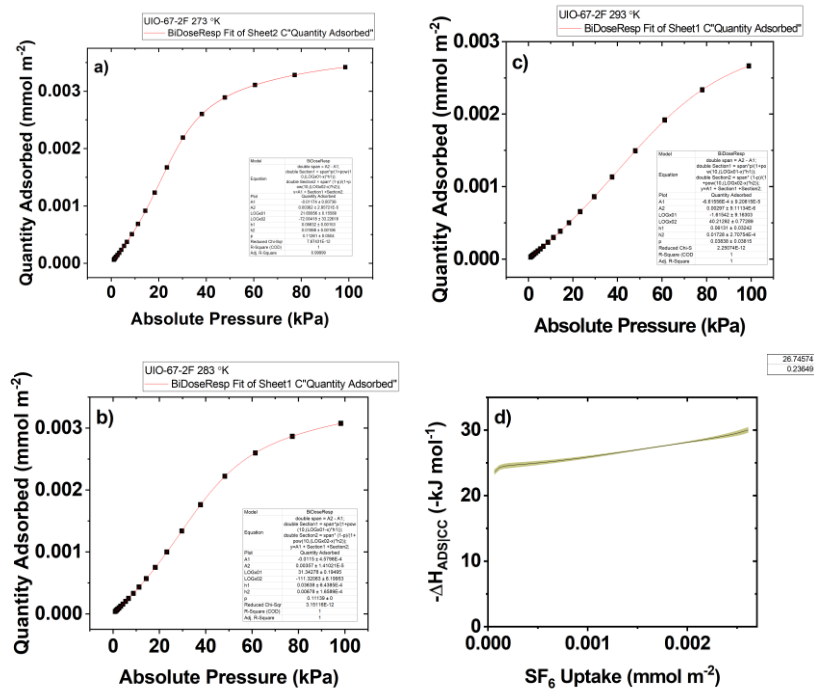


Fig S47. Adsorption isotherms of SF₆ onto UIO-67-F2 and fits at a) 0 °C, b) 10 °C, c) 20 °C, and d) isosteric enthalpy SF₆ adsorption onto UIO-67-F2 as a function of mmol SF₆ per m² sorbent (normalized by the BET specific surface area of the MOF). The standard error of the fitted isosteres is represented by the brown highlight

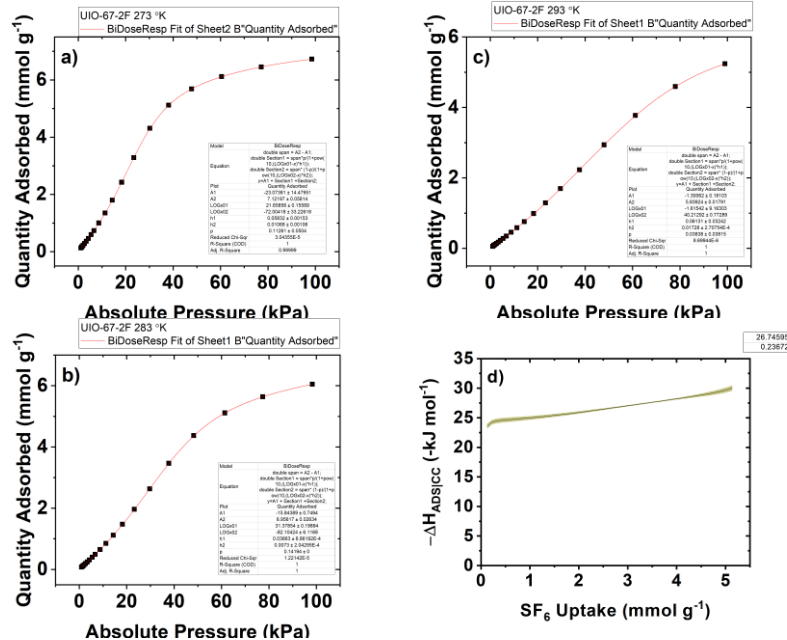


Fig S48. Adsorption isotherms of SF₆ onto UIO-67-F2 and fits at a) 0 °C, b) 10 °C, c) 20 °C, and d) isosteric enthalpy SF₆ adsorption onto UIO-67-F2 as a function of mmol SF₆ per g sorbent. The standard error of the fitted isosteres is represented by the brown highlight

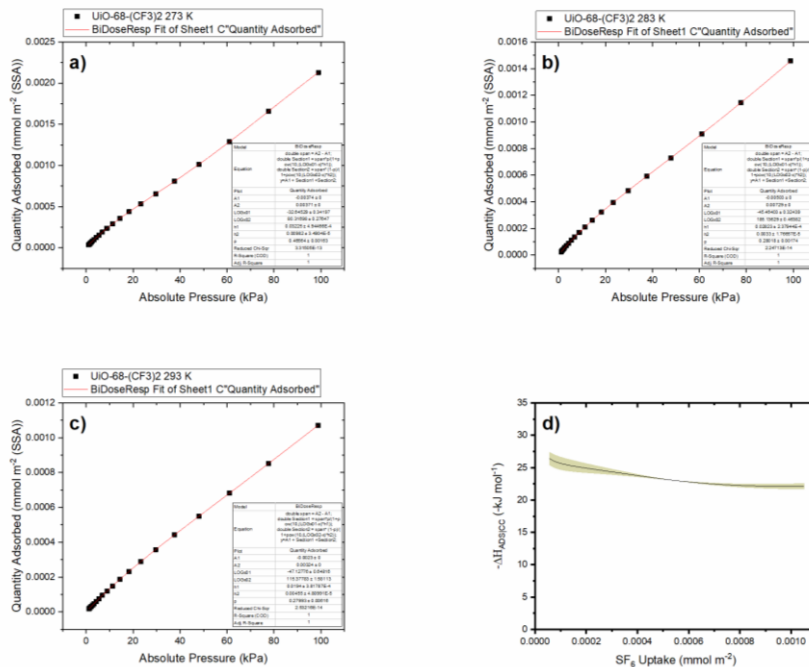


Fig S49. Adsorption isotherms of SF₆ onto UIO-67-(CF3)2 and fits at a) 0 °C, b) 10 °C, c) 20 °C, and d) isosteric enthalpy SF₆ adsorption onto UIO-67-(CF3)2 as a function of mmol SF₆ per m² sorbent (normalized by the BET specific surface area of the MOF). The standard error of the fitted isosteres is represented by the brown highlight.

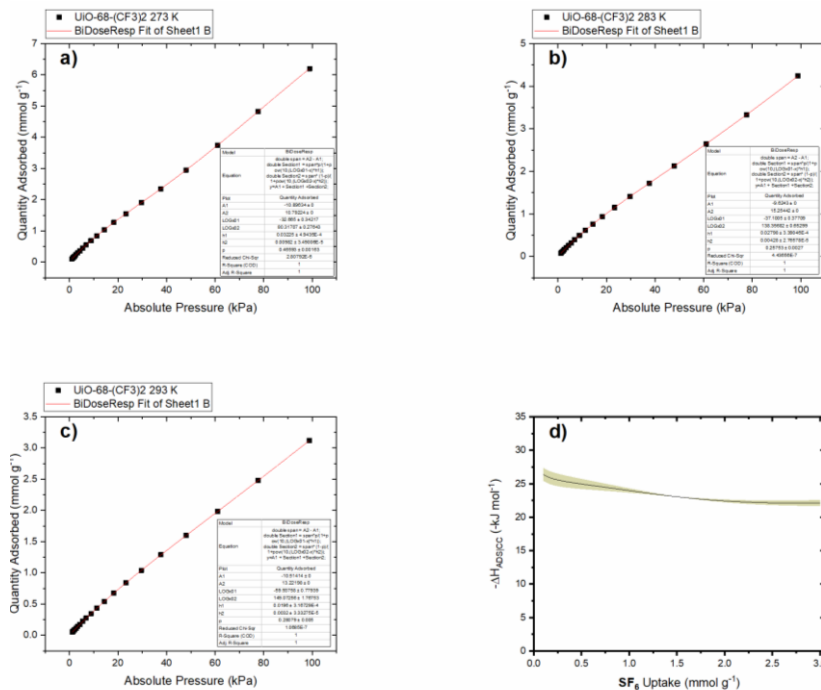


Fig S50. Adsorption isotherms of SF₆ onto UIO-67-(CF3)2 and fits at a) 0 °C, b) 10 °C, c) 20 °C, and d) isosteric enthalpy SF₆ adsorption onto UIO-67-(CF3)2 as a function of mmol SF₆ per g sorbent. The standard error of the fitted isosteres is represented by the brown highlight.

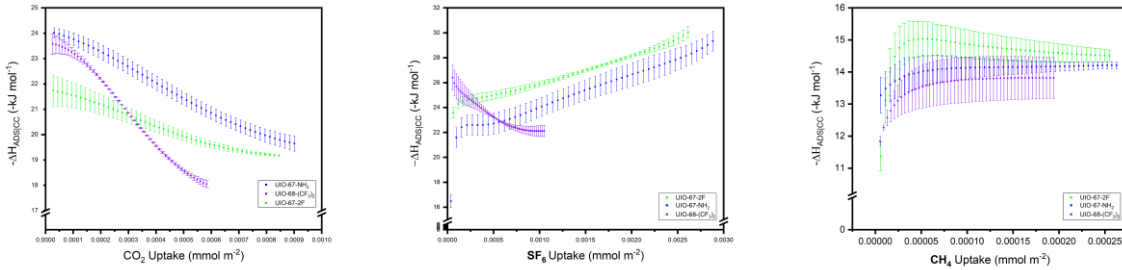


Fig S51. Isosteric enthalpies of (a) CO_2 , (b) SF_6 and, (c) CH_4 adsorption, normalized by surface area of each MOF (i.e., BET specific surface area). Vertical error bars are the standard error of the fitted isosteres for each data point.

S 14. Ideal Adsorbed Solution Theory

Theoretical selectivities for binary gas mixtures were constructed from measured single-component isotherms up to 100 kPa. The selectivity calculations were performed in accordance with the ideal adsorbed solution theory (IAST)⁸, implemented in Graphlast⁹. IAST⁸, was implemented in order to simulate selectivity in a gas mixture of species *i* and *j*, over the examined pressure range. The major steps in the application of IAST was as follows.

Experimentally acquired isotherms were fitted using the dual site Langmuir model (all N_2 , CH_4 , CO_2 isotherms) or a quadratic equation (SF_6 isotherms). These equations are denoted $n_i^o(P^o)$. These fitted isotherm equations can be integrated to, for dual site Langmuir,

$$\begin{aligned} \pi_n(P_n^o) &= \frac{RT}{A} \int_0^{P_n^o} q_n * \frac{K_n * P}{1 + K_n * P} + q_{n2} * \frac{K_{n2} * P}{1 + K_{n2} * P} d \ln(P) = \dots \\ &= \frac{RT}{A} \int_0^{P_n^o} \left(q_n * \frac{K_n * P}{1 + K_n * P} + q_{n2} * \frac{K_{n2} * P}{1 + K_{n2} * P} \right) * P^{-1} d P = \dots \\ &= \frac{RT}{A} [q_n * \log(1 + K_n * P) + q_{n2} * \log(1 + K_{n2})] \end{aligned}$$

For the quadratic equation,

$$\pi_n(P_n^o) = \frac{RT}{A} \int_0^{P_n^o} n_n^o(P) d \ln(P) = \dots = \frac{RT}{A} M * \log(1 + K_A * P_n^o + K_B * P_n^{o2})$$

The gas phase fraction of gas *i* and *j* are commonly chosen to industrially relevant partial pressures (N_2/CH_4 , CO_2/CH_4 , CO_2/N_2 , SF_6/N_2 as 0.5/0.5, 0.5/0.5, 0.15/0.85 and 0.1/0.9, respectively).

The IAST hypothetical gas pressure giving rise to the spreading pressure π ($P_i^o(\pi)$).

The adsorbed solution phase fraction, x_i , is guessed at this point ($0 < x_i < 1$). This guess is used to minimize the least square of the difference of adsorbed phase spreading pressures in each point P_i^o to satisfy

$$\sqrt{(\pi_i(P_i^o) - \pi_j(P_j^o))^2} = 0$$

The indexes, *i* and *j*, are best thought of as the first and second component. Which in the selectivity means selectivity of *i* from a mixture of *i* and *j*. As one has obtained adsorbed phase fractions (x_i , x_j), one can calculate selectivity by IAST of gas *i* from gas *j* in a mixture at partial pressures y_i , y_j , as

$$S_{ij} = \frac{x_i/y_i}{x_j/y_j} = \frac{P_j^o}{P_i^o}$$

At this point one can also calculate IAST-derived isotherms of the theoretical mixture as,

$$\frac{1}{n_{total}} = \frac{x_i}{n_i(P_i^o)} + \frac{x_j}{n_j(P_j^o)} \rightarrow n_{total}(P_i^o, P_j^o) = \left(\frac{x_i}{n_i(P_i^o)} + \frac{x_j}{n_j(P_j^o)} \right)^{-1}$$

The individual isotherms of the mixture are possible to calculate from the same equation.

The accuracy of the IAST has been evaluated by several sources and is considered lacking at low pressures. As such, a simple model known as selectivity by Henry's law, is appended as a supplementary model.

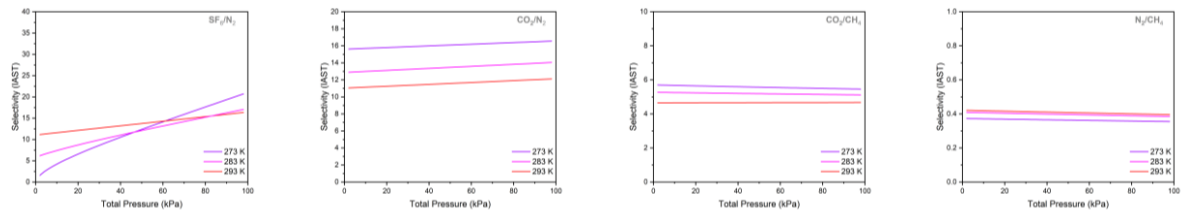


Fig S52. IAST selectivities of Uio-67-NH2, between 0 – 20 °C and up to 100 kPa for mixtures containing (a) SF₆/N₂ (10:90), (b) CO₂/N₂ (15:85), (c) CO₂/CH₄ (50:50), and (d) N₂/CH₄ (50:50).

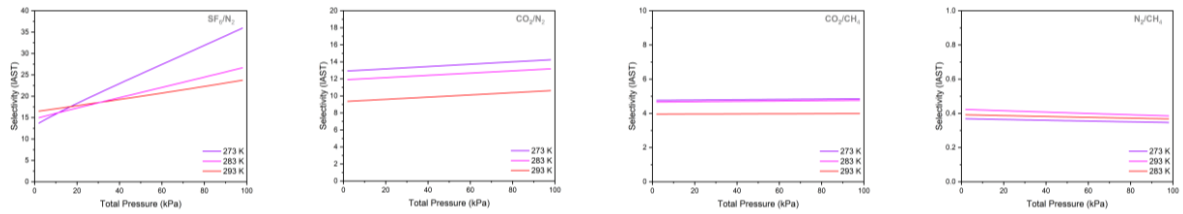


Fig S53. IAST selectivities of Uio-67-F2, between 0 – 20 °C and up to 100 kPa for mixtures containing (a) SF₆/N₂ (10:90), (b) CO₂/N₂ (15:85), (c) CO₂/CH₄ (50:50), and (d) N₂/CH₄ (50:50).

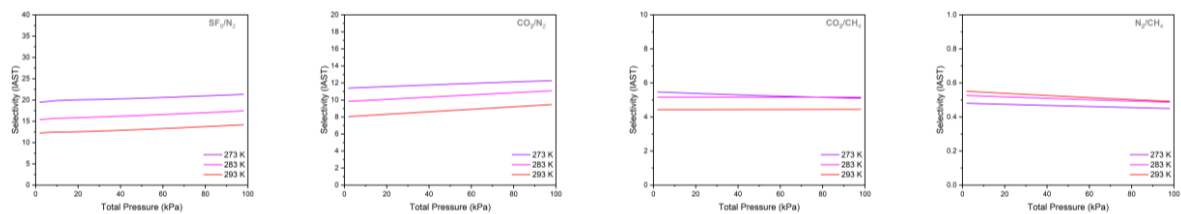


Fig S54. IAST selectivities of Uio-68-(CF₃)₂, between 0 – 20 °C and up to 100 kPa for mixtures containing (a) SF₆/N₂ (10:90), (b) CO₂/N₂ (15:85), (c) CO₂/CH₄ (50:50), and (d) N₂/CH₄ (50:50).

S 15. Ideal selectivity

Selectivity by Henry's constant, uses Henry's law constants to create a selectivity calculation which compares uptake at very low pressures. At very low pressures, adsorption follows Henry's law,

$$n_i = K_H * p$$

Where n_i is uptake of adsorbate i. p is the pressure, and K_H Henry's constant (units all depend on choice). In a binary mixture of species, A and B, selectivity (S) of A from B is calculated by,

$$S = \frac{K_H^A}{K_H^B}$$

And results are visible below in Fig. S45.

Henry's selectivity of CO₂/CH₄ and N₂/CH₄ range from very low, to virtually zero in all examined UiO MOFs.

CO₂/N₂ selectivity ranges between 10 – 15 in UiO-67-F2 and 12 – 17 in UiO-67-NH2 at 0 – 20 °C.

SF₆/N₂ selectivity ranges between 16 – 24 for UiO-67-NH2, 12 – 19 in UiO-68-(CF3)2, and 22 – 32 in UiO-67-F2. In all three cases between 20 and 0 °C in the Henry's law region of uptake (very low kPa). These results agree with the IAST simulated selectivity, the functionalization present in UiO-67-F2 seems to have an increasing effect on the selectivity of SF₆/N₂.

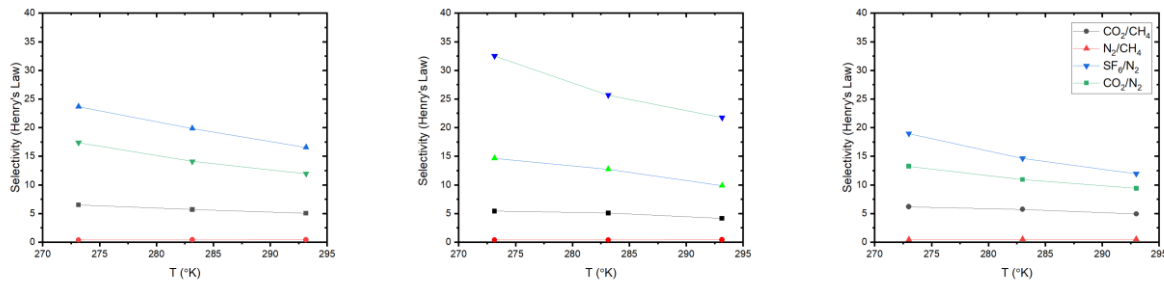


Fig S55. Ideal selectivities predicted using Henry's Law (a) UiO-67-NH2, (b) UiO-67-F2, and (c) UiO-68-(CF3)2.

S 16. Summary of sorption properties

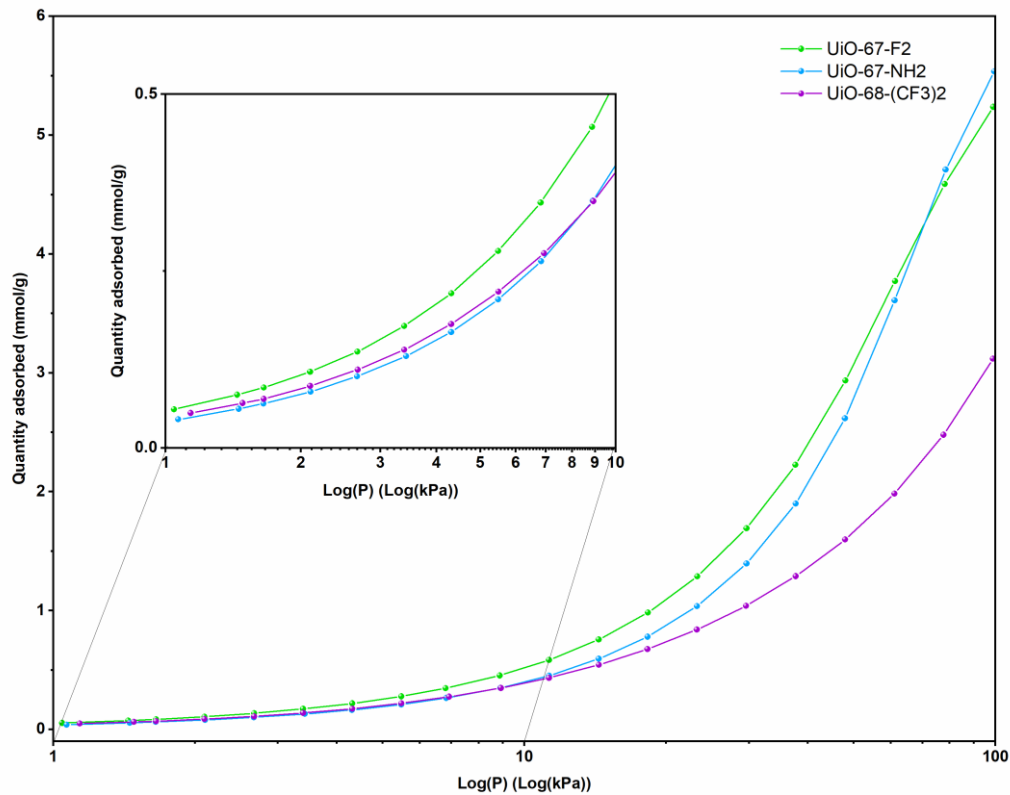


Fig S56. SF₆ uptake vs log(p) at 20 C for UiO-67-F2 (green), UiO-67-NH2 (blue), and UiO-68-(CF3)2 (purple). The region between 1 and 10 log(kPa) is magnified to visualize individual differences.

Table S13. Sorptive properties of UiO-67-NH2, UiO-67-F2, and UiO-68-(CF3)2.

	UiO-67-NH2	UiO-67-F2	UiO-68-(CF3)2
<i>Uptake</i> (100 kPa and 20 °C)			
N ₂ (cm ³ /g / mmol/m ²)	0.21 / 1.1 × 10 ⁻⁴	0.21 / 1.0 × 10 ⁻⁴	0.29 / 1.0 × 10 ⁻⁴
CO ₂ (cm ³ /g / mmol/m ²)	1.7 / 9.2 × 10 ⁻⁴	1.7 / 8.5 × 10 ⁻⁴	1.7 / 5.9 × 10 ⁻⁴
CH ₄ (cm ³ /g / mmol/m ²)	0.49 / 2.6 × 10 ⁻⁴	0.51 / 2.6 × 10 ⁻⁴	0.58 / 1.1 × 10 ⁻⁴
SF ₆ (cm ³ /g / mmol/m ²)	5.5 / 2.9 × 10 ⁻³	5.2 / 2.7 × 10 ⁻³	3.1 / 1.1 × 10 ⁻³
<i>Selectivity</i>			
IAST, SF ₆ /N ₂ , 10:90, 0 °C, 100 kPa	21	36	21
IAST, SF ₆ /N ₂ , 10:90, 20 °C, 100 kPa	16	24	14

Henry's Law, SF ₆ /N ₂ , 0 °C	24	33	19
Henry's Law, SF ₆ /N ₂ , 20 °C	17	22	12
Mean -ΔH_{ads}			
N ₂ (kJ/mol)	10.3 ± 0.7	11.3 ± 0.6	10.3 ± 0.54
CO ₂ (kJ/mol)	21.7 ± 0.26	20.3 ± 0.25	20.82 ± 0.09
CH ₄ (kJ/mol)	14.0 ± 0.29	14.6 ± 0.41	13.6 ± 0.63
SF ₆ (kJ/mol)	25.2 ± 0.83	26.7 ± 0.24	23.4 ± 0.38
Working capacity (10 – 100 kPa at 20 °C)			
SF ₆ (cm ³ /g / mmol/g)	106 / 4.7	115 / 5.2	61 / 2.7

Table S14. Comparative table UiO-67-NH₂, UiO-67-F2, and UiO-68-(CF₃)₂ with various other published MOFs available in literature.

	SF₆ uptake at 100 kPa (cm ³ /g)	Density. (g/cm ³)	Volumetric uptake (cm ³ /cm ³)	Temperature (°C)	Source
Cu ₃ (btc) ₂	107	0.965	103	25	¹⁰
UiO-67-NH ₂	124	0.777	96	20	This study
UiO-67-F2	117	0.726	85	20	This study
MIL-100(Fe)	66	0.961	63	25	¹⁰
Co ₂ (1,4-bdc) ₂ (dabco)	76	0.732	56	25	¹⁰
UiO-68-(CF ₃) ₂	70	0.654	46	20	This study
Zn ₄ O(dmcpz) ₃	57	0.605	34	25	¹⁰
DUT-9	52	0.646	34	25	¹⁰
CTH-18	44	1.486	65	20	¹¹
MIL-101(Cr)	45	0.961	14	25	¹⁰
Zn ₄ O(btb) ₂	70	0.315	22	25	¹⁰
SBMOF-1	23	1.624	37	25	¹²
UiO-67	84	0.723	61	20	This study

S 17. PFOA adsorption

The PFOA adsorption experiments were conducted on a Radleys Carousel 12 Plus Reaction Station (Saffron Walden, Essex, UK) and all glassware for the reaction station were dried in a vacuum oven at 250 °C for 24 h prior to the experiment. The activated MOFs (1 g/L) were briefly sonicated for 30 s in deionized water in the reactor tubes to disperse the materials. Varying amounts of a PFOA stock solution (3 232 mg/L) was thereafter added to the MOF suspensions (Tables S8 and S9) and the mixtures were stirred (~150 rpm) at 25 °C for 2.5 h. After the predetermined time, 1.5 mL of the solution was drawn from each tube and centrifuged at 5 000 rpm for 5 min, after which 0.9 mL of the supernatant was added to an NMR-tube along with 0.1 mL of a trifluoroethanol (TFE) solution (0.12 M in H₂O (H₂O/D₂O at 90:10 v/v)). A blank sample was prepared and treated the same way as the samples containing MOF.

Table S15. Summary of PFOA solutions used in UiO-67-F2.

C₀ (mg/L)	V_{H₂O} (mL)	V_{PFOA stock} (mL)	m_{UiO-67-F2} (mg)	pH
0	2.000	0	0	7
150	3.220	0.157	3.38	6
250	2.430	0.203	2.63	5
500	2.160	0.396	2.56	4
750	1.570	0.473	2.04	3
1 000	2.030	0.910	2.94	3
1 500	1.130	0.980	2.11	3
2 000	0.713	1.160	1.87	2
3 232	0	1.710	1.71	2
3 232 (Blank)	0	2.000	0	2

Table S16. Summary of PFOA solutions used in UiO-67.

C₀ (mg/L)	V_{H₂O} (mL)	V_{PFOA stock} (mL)	m_{UiO-67} (mg)	pH
500	1.340	0.244	1.58	4
750	1.050	0.318	1.37	3
1 000	1.660	0.742	2.40	3
1 500	0.836	0.724	1.56	3
2 000	0.774	1.260	2.03	2
3 232	0	1.770	1.77	2
3 232 (Blank)	0	2.000	0	2

S 17.1. Quantitative fluorine-19 nuclear magnetic resonance spectroscopy (^{19}F NMR)

^{19}F NMR spectra were recorded on a Bruker Avance III 600 MHz spectrometer (Billerica, MA, USA). Shimming was manually performed against ^1H NMR spectra, the relaxation delay was set to 30 s and 64 scans were collected for each sample. ^{19}F NMR spectra were collected within a range of -70 to -140 ppm in order to target the terminal CF_3 -groups of both the TFA internal standard and PFOA as well as the fluorine atoms (- CF_2 -) on the backbone of the PFOA molecules. The obtained spectra were processed by adjusting the chemical shift of the signal for the CF_3 -group of TFE to -76 ppm. The integrated intensity of the signals corresponding to the CF_3 -group of TFE and PFOA were compared in order to calculate the concentration of PFOA in the suspensions. Care in this step to recognize that the PFOA-solution has been diluted by 0.1 mL when placed into the NMR-tube, the uptake of adsorbate.

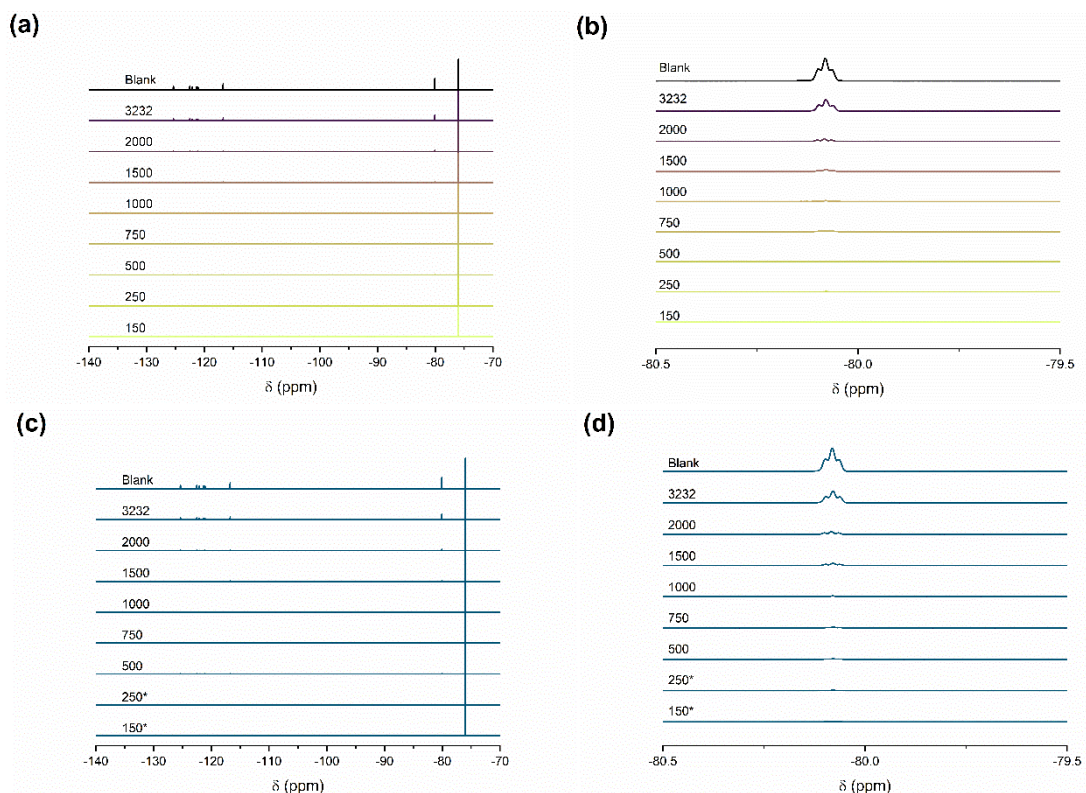


Fig S57. ^{19}F NMR spectra of aqueous PFOA solutions after MOF immersion for 2.5 h for (a–b) UiO-67-F2 and (c–d) UiO-67. (b), (d) pertain to magnified regions in (a) and (c). The solutions contained TFE as internal standard. *d) 150, 250 Samples fell outside detectable limits.

Table S17. Calculated PFOA uptake of UiO-67-F₂ as obtained from ¹⁹F NMR spectroscopy.

<i>C₀</i> (mg/L)	<i>Integral area</i> (CF ₃ -signal)		<i>PFOA uptake</i> (mg/g)
	TFE	PFOA	
150	944.7	3	0.148
250	461.2	3	0.245
500	293.3	3	0.486
750	155.2	3	0.716
1 000	88.5	3	0.928
1 500	54.2	3	1.330
2 000	31.1	3	1.630
3 232	11.7	3	1.680
3 232 (Blank)	5.5	3	0

Table S18. Calculated PFOA uptake of UiO-67 as obtained from ¹⁹F NMR spectroscopy

<i>C₀</i> (mg/L)	<i>Integral area</i> (CF ₃ -signal)		<i>PFOA uptake</i> (mg/g)
	TFE	PFOA	
500	494.0	3	0.489
750	86.1	3	0.695
1 000	46.2	3	0.872
1 500	22.3	3	1.120
2 000	15.2	3	1.260
3 232	8.4	3	1.100
3 232 (Blank)	5.5	3	0

The equilibrium PFOA uptake for UiO-67-F2 and UiO-67 were plotted and fit according to the Langmuir equation (**Eq. 14**):

$$q = q_m * \frac{K_L \cdot C}{1 + K_L \cdot C} \quad \text{Eq. 14}$$

Where q denotes the uptake (mg/g), q_m the maximum adsorption capacity (mg/g), K_L the adsorption equilibrium constant (L/mg), and C the concentration of adsorbate (mg/L).

As well as the Toth equation (**Eq. 15**):

$$q = q_m * \frac{K_L \cdot C}{1 + ((K_L \cdot C)^{b_0})^{1/b_0}} \quad \text{Eq. 15}$$

Where q denotes the uptake (mg/g), q_m the maximum adsorption capacity (mg/g), K_L the adsorption equilibrium constant (L/mg), and C the concentration of adsorbate (mg/L).

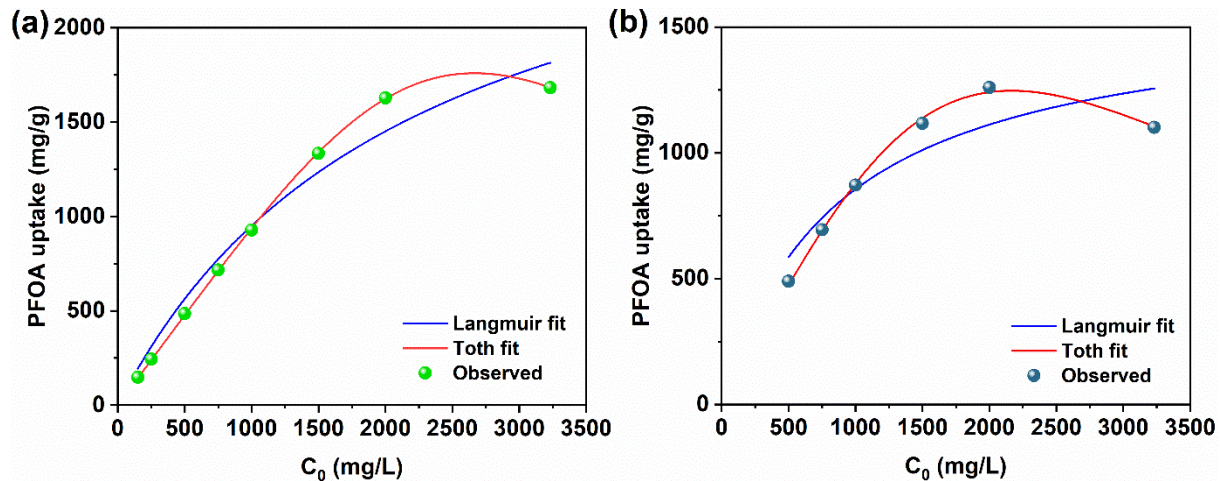


Fig S58. Equilibrium PFOA uptake of (a) UiO-67-F2 and (b) UiO-67 at 25 °C.

Table S19. Toth isotherm parameters for PFOA adsorption on UiO-67-F2 and UiO-67.

Parameters	UiO-67-F2	UiO-67
q (mg/g)	10,556.46	6,062.01
K_L	2.93×10^{-4}	3.94×10^{-4}
b_0	3.23	2.48
RMSE	7.7120	19.2596

Table S20. Langmuir isotherm parameters for PFOA adsorption on UiO-67-F2 and UiO-67.

Parameters	UiO-67-F2	UiO-67
q (mg/g)	3,059.94	1,589.12
K_L (L/mg)	4.51×10^{-4}	11.70×10^{-3}
RMSE	111.5354	131.1160

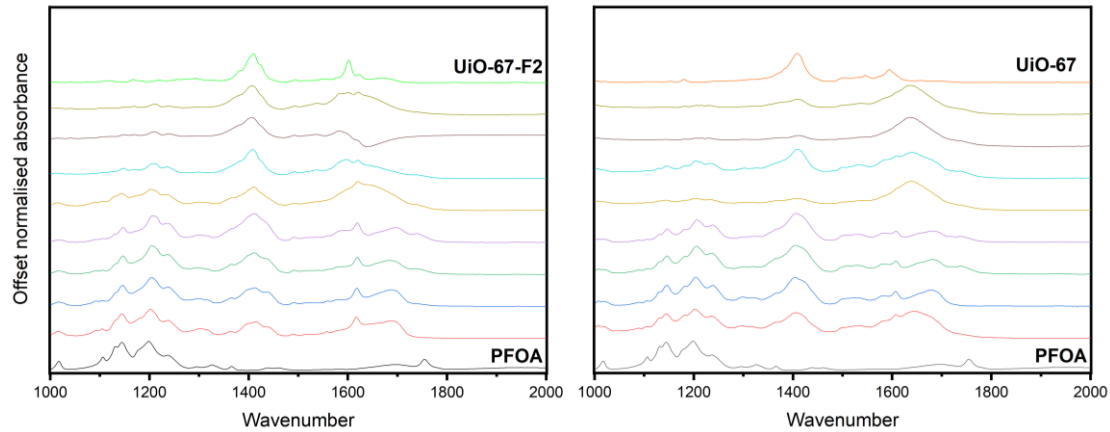


Fig S59. Stacked FT-IR spectra of (left) **UiO-67-F2** and (right) **UiO-67** after soaking in 150 – 3232 mg/L PFOA solutions (increasing from top to bottom) for 2.5 h. The first (i.e., top) and last (i.e., bottom) spectra represent the pristine **UiO**-MOFs and PFOA compound, respectively.

The recyclability of **UiO-67-F2** was also examined using PXRD. Sample after PFOA adsorption were freeze-dried, and degassed under dynamic vacuum for 10 h (40 °C), after which they were washed with acetonitrile, and separated using a centrifuge (3 x 45 mL).

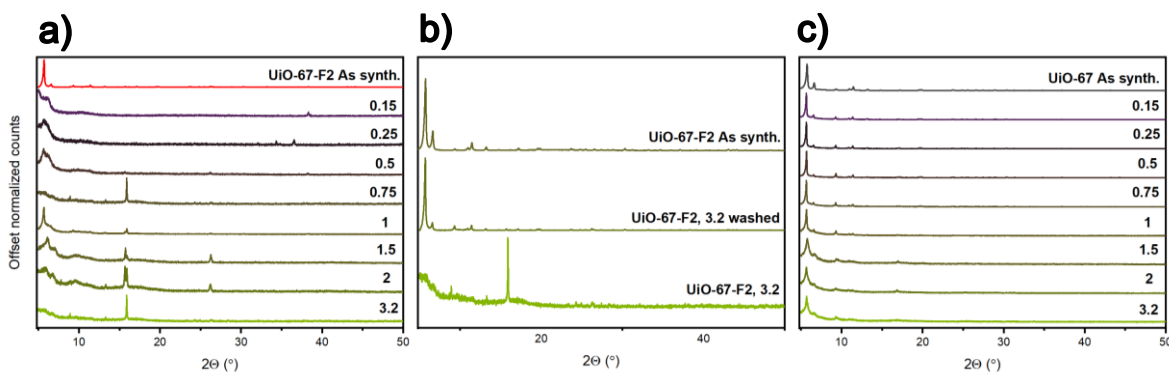


Fig S60. Stacked PXRD diffractograms of **UiO-67-F2** a-b) after soaking in 150 – 3232 mg/L PFOA for 2.5 h and b-c) after washing in acetonitrile.

Table S21. Summary of porosity and PFOA adsorption in UiO-67, UiO-67-F2, as well as other MOFs from published literature.

Material	SSA _{BET} (g/m ²)	V _{tot} (cm ³ /g)	Pore size (Å)	PFOA uptake (mg/g)	pH	C ₀ (g/L)	MOF (g/L)	Ref.
UiO-67-F2	1966	0.78	10.9, 13.5 ^d	928	3	1000	1	This study
UiO-67	2126	0.98	10.9 ^d	872	3	1000	1	This study
PCN-999	1696	0.79	14, 22 ^d	764	-	1000	1	¹³
MIL-101(Cr)-QDMEN	1530	-	-	754	5	1000	0.1	¹⁴
Fe-BTC	1051	1.34	-	548	3.3	1000	1	^{15,16}
MIL-101(Cr)-DMEN	1692	-	-	493	5	1000	0.1	¹⁴
NU-1000	2225	1.56	13, 33 ^d	507	-	0.1	0.2	¹⁷
MIL-101(Fe)	1811	1.8	29, 34	370	3.3	1000	1	^{15,16}
UiO-66-F4	682	0.5	-	467	4	335	1	^{15,18}
MIL-101(Cr)	2560	1.68	29, 34	460	5	1000	0.1	¹⁵
MIL-100(Fe)	1237	1.25	25, 29	349	3.3	1000	1	^{15,16}
UiO-66	1580	0.56	6	388	4	500	1	¹⁵
MIL-96-RHPAM2	75	0.24	-	340	-	1000	1	¹⁵
MIL-101(Cr)-NH ₂	1195	2.0	14, 25	290	5	1000	0.1	¹⁴
Mn-BTC	1527	0.61	1.6 ^d	130	3.3	1000	1	^{15,16}
Cu-BTC	1429	0.31	11, 3, 5 ^d	95	3.3	1000	1	^{15,16}

^dDFT pore size calculated from N₂ isotherms recorded at -196 °C.

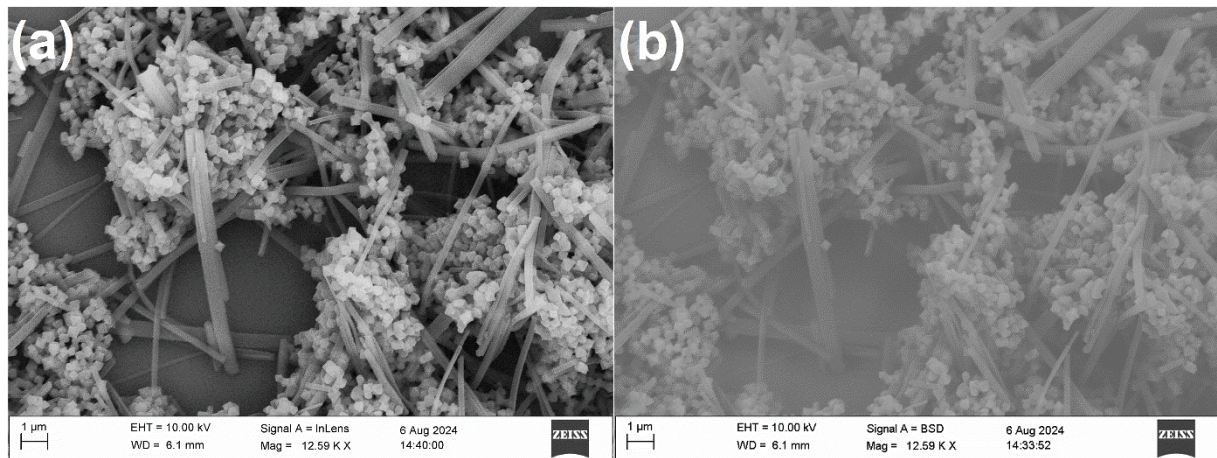


Fig S61. SEM images of UiO-67-F2 after soaking in 3232 mg/L PFOA for 2.5h recorded at (a) 10 kV using an in-lens (BSE) detector and (b) 10 kV using a 4-quadrant BSD detector in compositional mode.

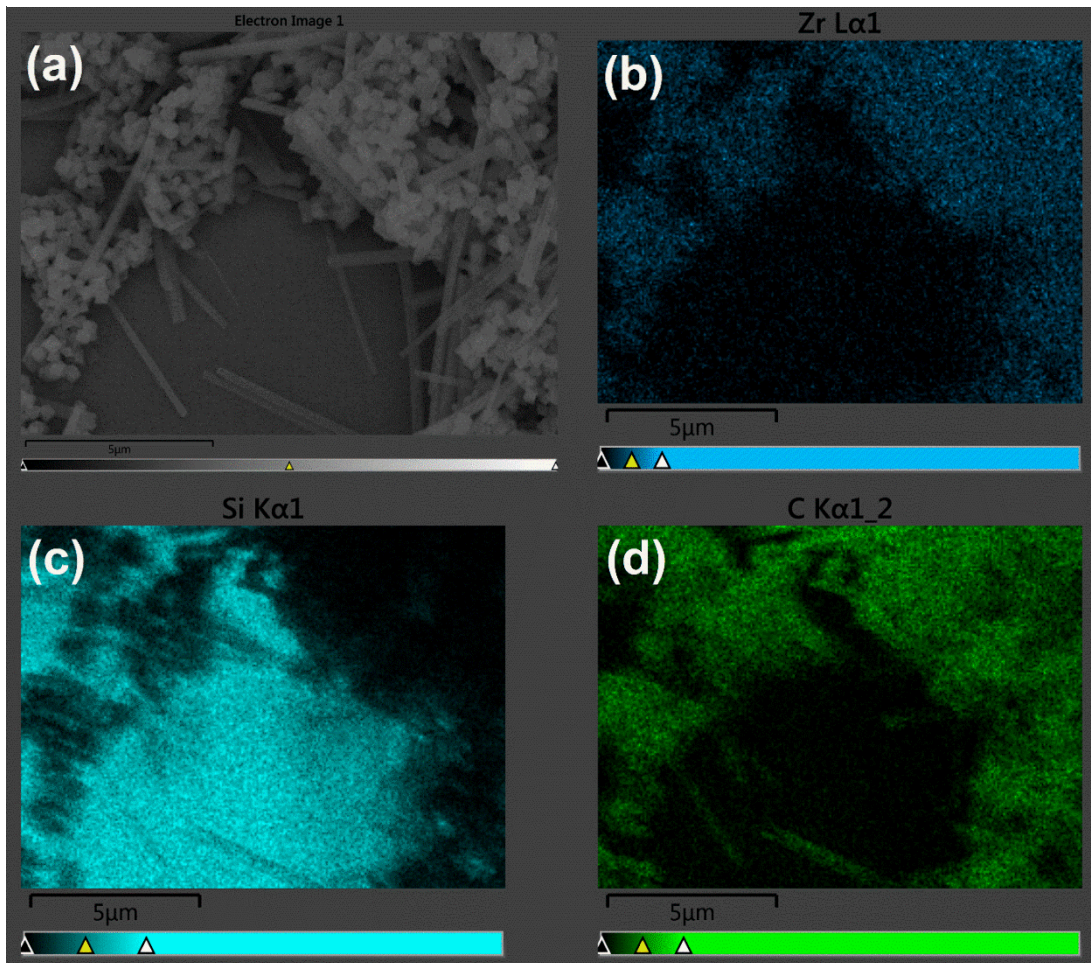


Fig S62. (a) SEM images of UiO-67-F2 after soaking in 3232 mg/L PFOA for 2.5h recorded at 10 kV using an in-lens (BSE) detector and EDX maps of (b) Zr L α 1 signal, (c) Si K α 1 signal, (d) C K α 1,2 signal.

References

- 1 P. M. Stanley, J. Haimerl, C. Thomas, A. Ursstoeger, M. Schuster, N. B. Shustova, A. Casini, B. Rieger, J. Warnan and R. A. Fischer, *Angewandte Chemie International Edition*, 2021, **60**, 17854–17860.
- 2 G. Kaur, S. Øien-Ødegaard, A. Lazzarini, S. M. Chavan, S. Bordiga, K. P. Lillerud and U. Olsbye, *Cryst Growth Des*, 2019, **19**, 4246–4251.
- 3 H. Wang, L. Yu, Y. Lin, J. Peng, S. J. Teat, L. J. Williams and J. Li, *Inorg Chem*, 2020, **59**, 4167–4171.
- 4 H. M. Rietveld, *J Appl Crystallogr*, 1969, **2**, 65–71.
- 5 G. C. Shearer, S. Chavan, S. Bordiga, S. Svelle, U. Olsbye and K. P. Lillerud, *Chemistry of Materials*, 2016, **28**, 3749–3761.
- 6 J. W. M. Osterrieth, J. Rampersad, D. Madden, N. Rampal, L. Skoric, B. Connolly, M. D. Allendorf, V. Stavila, J. L. Snider, R. Ameloot, J. Marreiros, C. Ania, D. Azevedo, E. Vilarrasa-Garcia, B. F. Santos, X. Bu, Z. Chang, H. Bunzen, N. R. Champness, S. L. Griffin, B. Chen, R. Lin, B. Coasne, S. Cohen, J. C. Moreton, Y. J. Colón, L. Chen, R. Clowes, F. Coudert, Y. Cui, B. Hou, D. M. D'Alessandro, P. W. Doheny, M. Dincă, C. Sun, C. Doonan, M. T. Huxley, J. D. Evans, P. Falcaro, R. Ricco, O. Farha, K. B. Idrees, T. Islamoglu, P. Feng, H. Yang, R. S. Organ, D. Bara, S. Furukawa, E. Sanchez, J. Gascon, S. Telalović, S. K. Ghosh, S. Mukherjee, M. R. Hill, M. M. Sadiq, P. Horcajada, P. Salcedo-Abraira, K. Kaneko, R. Kukobat, J. Kenvin, S. Keskin, S. Kitagawa, K. Otake, R. P. Lively, S. J. A. DeWitt, P. Llewellyn, B. V. Lotsch, S. T. Emmerling, A. M. Pütz, C. Martí-Gastaldo, N. M. Padial, J. García-Martínez, N. Linares, D. MasPOCH, J. A. Suárez del Pino, P. Moghadam, R. Oktavian, R. E. Morris, P. S. Wheatley, J. Navarro, C. Petit, D. Danaci, M. J. Rosseinsky, A. P. Katsoulidis, M. Schröder, X. Han, S. Yang, C. Serre, G. Mouchaham, D. S. Sholl, R. Thyagarajan, D. Siderius, R. Q. Snurr, R. B. Goncalves, S. Telfer, S. J. Lee, V. P. Ting, J. L. Rowlandson, T. Uemura, T. Iiyuka, M. A. van der Veen, D. Rega, V. Van Speybroeck, S. M. J. Rogge, A. Lamaire, K. S. Walton, L. W. Bingel, S. Wuttke, J. Andreo, O. Yaghi, B. Zhang, C. T. Yavuz, T. S. Nguyen, F. Zamora, C. Montoro, H. Zhou, A. Kirchon and D. Fairen-Jimenez, *Advanced Materials*, 2022, **34**, 2201502.
- 7 F. Rouquerol, J. Rouquerol and K. Sing, eds. F. Rouquerol, J. Rouquerol and K. B. T.-A. by P. and P. S. Sing, Academic Press, London, 1999, pp. 27–50.
- 8 A. L. Myers and J. M. Prausnitz, *AIChE Journal*, 1965, **11**, 121–127.
- 9 E. Dautzenberg, S. van Hurne, M. M. J. Smulders and L. C. P. M. de Smet, *Comput Phys Commun*, 2022, **280**, 108494.
- 10 I. Senkovska, E. Barea, J. A. R. Navarro and S. Kaskel, *Microporous and Mesoporous Materials*, 2012, **156**, 115–120.
- 11 F. M. Amombo Noa, O. Cheung, M. Åhlén, E. Ahlberg, P. Nehla, G. Salazar-Alvarez, S. Ershadrad, B. Sanyal and L. Öhrström, *Chemical Communications*, 2023, **59**, 2106–2109.
- 12 T. Wang, M. Chang, T. Yan, Y. Ying, Q. Yang and D. Liu, *Ind Eng Chem Res*, 2021, **60**, 5976–5983.

- 13 R.-R. Liang, S. Xu, Z. Han, Y. Yang, K.-Y. Wang, Z. Huang, J. Rushlow, P. Cai, P. Samorì and H.-C. Zhou, *J Am Chem Soc*, 2024, **146**, 9811–9818.
- 14 K. Liu, S. Zhang, X. Hu, K. Zhang, A. Roy and G. Yu, *Environ Sci Technol*, 2015, **49**, 8657–8665.
- 15 R. Li, N. N. Adarsh, H. Lu and M. Wriedt, *Matter*, 2022, **5**, 3161–3193.
- 16 Y. Yang, Z. Zheng, W. Ji, J. Xu and X. Zhang, *J Hazard Mater*, 2020, **395**, 122686.
- 17 R. Li, S. Alomari, R. Stanton, M. C. Wasson, T. Islamoglu, O. K. Farha, T. M. Holsen, S. M. Thagard, D. J. Trivedi and M. Wriedt, *Chemistry of Materials*, 2021, **33**, 3276–3285.
- 18 K. Sini, D. Bourgeois, M. Idouhar, M. Carboni and D. Meyer, *New Journal of Chemistry*, 2018, **42**, 17889–17894.